



# Nitric acid-assisted growth of InVO<sub>4</sub> nanobelts on protonated ultrathin C<sub>3</sub>N<sub>4</sub> nanosheets as an S-scheme photocatalyst with tunable oxygen vacancies for boosting CO<sub>2</sub> conversion

Li Wang<sup>a,1</sup>, Deli Chen<sup>a,1</sup>, Shuqi Miao<sup>a</sup>, Fang Chen<sup>b,\*</sup>, Changfa Guo<sup>a,\*</sup>, Pengcheng Ye<sup>a</sup>, Jiqiang Ning<sup>c</sup>, Yijun Zhong<sup>a</sup>, Yong Hu<sup>a,b,\*</sup>

<sup>a</sup> Key Laboratory of the Ministry of Education for Advanced Catalysis Materials, Department of Chemistry, Zhejiang Normal University, Jinhua 321004, PR China

<sup>b</sup> Hangzhou Institute of Advanced Studies, Zhejiang Normal University, Hangzhou 311231, PR China

<sup>c</sup> Department of Optical Science and Engineering, Fudan University, Shanghai 200438, PR China

## ARTICLE INFO

### Keywords:

C<sub>3</sub>N<sub>4</sub>  
InVO<sub>4</sub>  
Oxygen vacancy  
Protonation  
CO<sub>2</sub> photoreduction

## ABSTRACT

Engineering bulk defects and surface modifications are effective strategies to facilitate carriers separation and achieve high-efficiency photocatalysis, but it is challenging to realize the integrated regulation of the two aspects. Herein, we report an S-scheme heterojunction with tunable oxygen vacancies (Vo) via *in-situ* growth of InVO<sub>4</sub> nanobelts on protonated ultrathin C<sub>3</sub>N<sub>4</sub> nanosheets (p-C<sub>3</sub>N<sub>4</sub>/InVO<sub>4</sub>) assisted by nitric acid for efficient CO<sub>2</sub> photoreduction. The nitric acid plays three roles in the synthetic process: providing protonation sources for the p-C<sub>3</sub>N<sub>4</sub>, assisting the growth of InVO<sub>4</sub> nanobelts on p-C<sub>3</sub>N<sub>4</sub>, and facilitating the formation of Vo in InVO<sub>4</sub>. Intriguingly, the Vo content is tuned by varying the amount of C<sub>3</sub>N<sub>4</sub> which reduces free H<sup>+</sup> concentration and increases the electron density around V in VO<sub>4</sub><sup>3-</sup>, leading to a trade-off effect on Vo formation and thus a volcano-shaped evolution profile of Vo content. The introduction of Vo reduces the band gap of InVO<sub>4</sub> and enhances the n-type conductivity, expediting the interfacial charge transfer in terms of the S-scheme pathway. Besides, the protonation of C<sub>3</sub>N<sub>4</sub> improves electrical conductivity, promotes the adsorption and activation of CO<sub>2</sub> molecules, and thermodynamically favours the conversion to CO. Due to the composite effect of Vo and protonation in the S-scheme system, the optimized p-C<sub>3</sub>N<sub>4</sub>/InVO<sub>4</sub> hetero-nanosheet displays dramatically boosted photocatalytic CO<sub>2</sub> reduction activity with a CO production rate of 14.05 μmol g<sup>-1</sup> h<sup>-1</sup>, 6.03 and 3.23 times higher than that of bare InVO<sub>4</sub> and p-C<sub>3</sub>N<sub>4</sub>, respectively. This work provides new platforms for the development of efficient photocatalysts by integrated refining of structure defects and surface modification in constructing heterostructures.

## 1. Introduction

The accelerated depletion of fossil fuels makes rapid growth of anthropogenic CO<sub>2</sub> emission, resulting in abiding environmental issues and energy crisis [1-5]. An ideal method to alleviate these problems is recycling CO<sub>2</sub> into ponderable chemicals such as CH<sub>4</sub>, CO, and so on [6]. Photocatalytic CO<sub>2</sub> reduction reaction (CO<sub>2</sub>RR), which takes advantage of solar energy as the reaction-driving force, is a promising approach to achieving the conversion [7,8]. However, CO<sub>2</sub>RR is a thermodynamically uphill process initiated at a low reduction potential (≤ -0.24 V vs. normalized hydrogen electrode, NHE, at pH = 7), and cannot be activated on most semiconductors. Since the pioneering report in 1979 [9],

many semiconductor photocatalysts have been synthesized to boost CO<sub>2</sub>RR activity. Unfortunately, most reported semiconductors show relatively low catalytic activity, which is closely associated with fixed band structures, rapid recombination of photogenerated carriers, as well as sluggish surface reaction kinetics [10,11].

To boost photocatalytic CO<sub>2</sub>RR activity, a variety of strategies have been developed, such as size regulation, defect engineering, heteroatom doping, loading cocatalysts, and constructing heterojunctions [12-19]. Among them, heterojunctions containing two and more semiconductors with different band gaps (E<sub>g</sub>), band edge positions, and abundant heterointerfaces have many merits for photocatalysis: (i) extending solar spectrum response and reinforcing the adsorption capacity; (ii)

\* Corresponding authors.

E-mail addresses: [chenfang@zjnu.edu.cn](mailto:chenfang@zjnu.edu.cn) (F. Chen), [changfa.guo@zjnu.edu.cn](mailto:changfa.guo@zjnu.edu.cn) (C. Guo), [yonghu@zjnu.edu.cn](mailto:yonghu@zjnu.edu.cn) (Y. Hu).

<sup>1</sup> These authors contributed equally to this work.

facilitating the interfacial transfer of photogenerated carriers and reducing the combination rate; (iii) spatial separation of redox-active sites boosts the forward reactions whilst suppresses the backward ones [20]. In the previous reports [21–23], the construction of Z-scheme systems is deemed as an efficacious way of CO<sub>2</sub> photoreduction, since photoexcited electrons are left in more negative conduction bands with high reduction ability. Typically, traditional and all-solid-state Z-scheme systems require appropriate electron mediators assisting electron transfer between two semiconductors, such as redox ion pairs of IO<sub>3</sub><sup>-</sup>/I<sup>-</sup>, Fe<sup>3+</sup>/Fe<sup>2+</sup>, and NO<sub>3</sub><sup>-</sup>/NO<sub>2</sub><sup>-</sup> and noble metal nanoparticles [23,24]. Despite improving photoactivity, they often result in the decrease of photo-absorption capacity and weak stability of whole photocatalysis systems. Moreover, noble metal nanoparticles as electron mediators make photocatalysis systems complex, costly, and suffer from a wide variety of reverse reactions between mediators and host photocatalysts [25]. Alternatively, the construction of the S-scheme systems comprising oxidation and reduction photocatalysts is proposed to address the above intrinsic blemishes [26]. In past years, a huge number of S-scheme heterojunctions were developed for CO<sub>2</sub> photoreduction [19,27,28]. However, the photocatalytic activity is still restricted mainly due to insufficient interfacial charge transfer. The recent reports suggest that engineering structure defects are an effective strategy for enhancing interfacial charge transfer [29,30]. For example, Chen et al. reported that the interfacial oxygen vacancy (Vo) serves as electron-transport channels, facilitating the separation of charge carriers, and inducing more electrons to participate in surface reduction reactions [29]. Zhao et al. designed a Vo-assisting 2D/2D Z-scheme BiO<sub>1-x</sub>Br/C<sub>3</sub>N<sub>4</sub> nanocomposite and found that Vo acts as a mediator capturing and shuttling electrons, accelerating the separation of photogenerated carriers [30]. Therefore, defect engineering of heterojunctions holds great potential for further improvement of photocatalytic activity.

Graphitic carbon nitride (C<sub>3</sub>N<sub>4</sub>), a metal-free semiconductor material, has stimulated tremendous research interest for photocatalytic hydrogen evolution and CO<sub>2</sub> conversion, owing to its many merits such as visible-light-driven E<sub>g</sub>, high conduction band minimum (CBM) position (-0.87 eV vs. NHE, pH = 7), environmental benignity, good thermal and chemical stability, cost-effectiveness, and easy preparation [31,32]. However, the electron localization in aromatic structures results in low electrical conductivity and thus easy recombination of photogenerated carriers, which together with confined active sites causes relatively low catalytic activity towards CO<sub>2</sub>RR. To this end, several strategies including layer number down, heteroatomic doping, and surface modification are proposed [31–33]. Recently, the protonation by hydrogen bonding with lone pair electrons of the nitrogen is suggested as a facile and effective surface modification method to delocalize in-plane electrons of C<sub>3</sub>N<sub>4</sub>. It is found that the protonation of C<sub>3</sub>N<sub>4</sub> not only improves dispersion and increases specific surface area, but also enables an adjustment of E<sub>g</sub> and electrical conductivity, promoting photocatalytic activity [34–36]. Therefore, it is speculated that the coupling of protonated C<sub>3</sub>N<sub>4</sub> (p-C<sub>3</sub>N<sub>4</sub>) and other semiconductors with controllable structure defects is an effective strategy of enhancing interfacial contact and electronic interactions between components and further boosting photocatalytic activity. However, the construction of p-C<sub>3</sub>N<sub>4</sub>-based heterojunctions, as well as the composite effects of protonation and structure defects such as Vo, is rarely reported. Furthermore, the understanding of the roles of protonation in surface reactions is scarce.

Inspired by this, we have elaborately designed an S-scheme heterojunction via in-situ growth of InVO<sub>4</sub> nanobelts with tunable Vo on protonated ultrathin C<sub>3</sub>N<sub>4</sub> nanosheets (p-C<sub>3</sub>N<sub>4</sub>/InVO<sub>4</sub>) for photocatalytic CO<sub>2</sub>RR. In this case, InVO<sub>4</sub> is chosen as the component due to its various advantages as follows [37–39]: (1) Suitable bandgap (~2.5 eV), enabling it to absorb visible light. (2) The band edge positions (CBM: -0.05 and VBM: 2.49 eV vs. NHE, pH = 7) can match with those of C<sub>3</sub>N<sub>4</sub> to carry out heterogeneous photocatalysis of CO<sub>2</sub> and H<sub>2</sub>O. (3) High chemical stability derived from the stable InO<sub>6</sub> octahedra and VO<sub>4</sub> tetrahedra as building blocks of the crystal structures. Nonetheless,

InVO<sub>4</sub> as a direct bandgap semiconductor suffers from serious recombination of photogenerated charge carriers, resulting in relatively low photocatalytic activity. Constructing heterostructures is an effective method of promoting photocatalysis efficiency. Therefore, the C<sub>3</sub>N<sub>4</sub>/InVO<sub>4</sub> heterostructure is chosen as a model photocatalyst to demonstrate the potential of protonated C<sub>3</sub>N<sub>4</sub>-based heterostructures on photocatalysis. The optimized p-C<sub>3</sub>N<sub>4</sub>/InVO<sub>4</sub> sample with abundant Vo displays remarkably enhanced photocatalytic CO<sub>2</sub>RR activity compared with single-component counterparts. The enhanced photoactivity is attributed to the composite effects of Vo and protonation in the S-scheme systems, which not only facilitates the separation and transfer of photogenerated carriers, but also promotes the adsorption and activation of CO<sub>2</sub> as well as the conversion to CO.

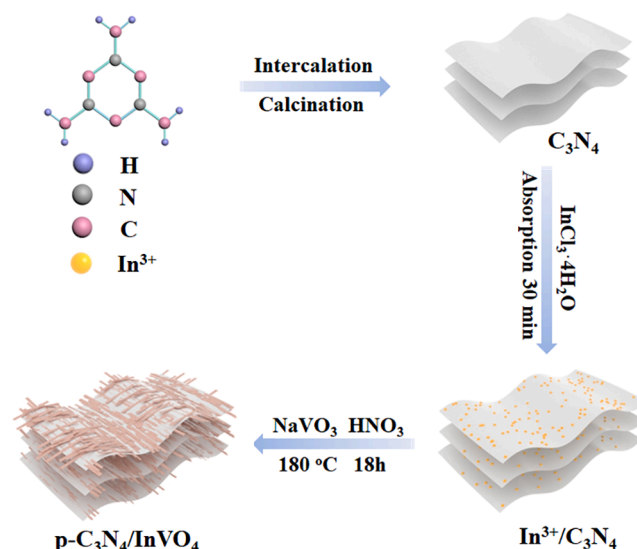
## 2. Experimental section

### 2.1. Material preparation

**Synthesis of C<sub>3</sub>N<sub>4</sub> nanosheet precursors:** The precursor was synthesized via a modified hydrothermal method [40,41]. 500 mg of melamine and 320 μL of phosphorous acid were dispersed in 50 mL of distilled water at 80 °C in a thermostatic water bath with vigorous magnetic stirring for 1 h. The resulting solution was then transferred into a 50 mL Teflon-lined autoclave and kept at 180 °C for 10 h. After cooled down to room temperature, the product was collected by centrifugation, washed with distilled water several times until the pH value of the solution reaches 7, and dried at 60 °C in an oven. The mass of the obtained sample was 450 mg.

**Synthesis of ultrathin C<sub>3</sub>N<sub>4</sub> nanosheets:** The as-prepared C<sub>3</sub>N<sub>4</sub> precursor was first dispersed into a mixed solvent of glycerol (5 mL) and ethanol (15 mL), and then refluxed at 90 °C for 3 h. After cooled down, the precipitate was collected by centrifugation and washed with ethanol for three times, and then dried at 60 °C. Finally, the resultant was calcined at 500 °C in the air for 2 h with a ramp rate of 2 °C/min. The mass of the obtained sample was 34 mg.

**Synthesis of p-C<sub>3</sub>N<sub>4</sub>/InVO<sub>4</sub> hetero-nanosheets:** Firstly, 1.0 mmol of InCl<sub>3</sub>·4H<sub>2</sub>O and a certain amount of ultrathin C<sub>3</sub>N<sub>4</sub> nanosheets were added into 10 mL of distilled water under vigorous stirring to form solution A. 1.0 mmol of NaVO<sub>3</sub> was dispersed in 20 mL of distilled water under stirring for 30 min to form solution B. Then, solution B was slowly added to solution A under stirring. The pH value of the mixed solution was adjusted to 1 ~ 2 by stepwise adding a certain amount of nitric acid (5.3 M). The mixture was then transferred into a Teflon-lined autoclave



Scheme 1. The synthetic process of the p-C<sub>3</sub>N<sub>4</sub>/InVO<sub>4</sub> hetero-nanosheets.

and maintained at 180 °C for 18 h. The product was collected by centrifugation and washed with water and ethanol three times, respectively, and dried at 60 °C for overnight. The addition amount of C<sub>3</sub>N<sub>4</sub> was set as 0, 30, 50, and 70 mg, the obtained sample was named as InVO<sub>4</sub> (x = 0) and p-C<sub>3</sub>N<sub>4</sub>/InVO<sub>4</sub>-x (x = 3, 5, and 7, respectively). As a comparison, the g-C<sub>3</sub>N<sub>4</sub>/InVO<sub>4</sub>-5 is prepared without the presence of dilute nitric acid, and InVO<sub>4</sub>-o is prepared without the addition of C<sub>3</sub>N<sub>4</sub> nanosheets and dilute nitric acid, according to the same procedures. The mass of the obtained sample was 125 mg.

**Synthesis of protonated C<sub>3</sub>N<sub>4</sub> nanosheets:** 50 mg of ultrathin C<sub>3</sub>N<sub>4</sub> nanosheets was added into 30 mL of distilled water under vigorous stirring for 30 min to form a homogeneous solution. Then, the pH value of the solution was adjusted to 1 ~ 2 by stepwise adding a certain amount of nitric acid (5.3 M). The mixture was transferred into a Teflon-lined autoclave and maintained at 180 °C for 18 h. The product was collected by centrifugation and washed with water and ethanol three times, respectively, and dried at 60 °C for overnight. The obtained sample was denoted as p-C<sub>3</sub>N<sub>4</sub> (mass: 45 mg).

**Synthesis of the mechanically mixed composite of p-C<sub>3</sub>N<sub>4</sub> and InVO<sub>4</sub> nanosheets:** 50 mg of as prepared ultrathin p-C<sub>3</sub>N<sub>4</sub> nanosheets and 100 mg bare InVO<sub>4</sub> were grinded together, and the as-obtained sample was labeled as p-C<sub>3</sub>N<sub>4</sub> + InVO<sub>4</sub>-5 (mass: 150 mg).

**Synthesis of InVO<sub>4</sub> without Vo:** The bare InVO<sub>4</sub> (100 mg) was calcined in the air at 250 °C for 4 h with a ramp rate of 2 °C/min, the obtained sample was labeled as InVO<sub>4</sub>-c (mass: 95 mg).

**Synthesis of InVO<sub>4</sub> with abundant Vo:** 100 mg of bare InVO<sub>4</sub> was immersed in 0.05 M NaBH<sub>4</sub> aqueous solution at room temperature for 1 h [42], the as-obtained sample is labeled as InVO<sub>4</sub>-r (mass: 95 mg).

**Synthesis of p-C<sub>3</sub>N<sub>4</sub>/InVO<sub>4</sub>-5 without Vo:** The p-C<sub>3</sub>N<sub>4</sub>/InVO<sub>4</sub>-5 (100 mg) was calcined in the air at 250 °C for 4 h, the obtained sample was labeled as p-C<sub>3</sub>N<sub>4</sub>/InVO<sub>4</sub>-5-c (mass: 95 mg).

## 2.2. Material characterizations

X-ray diffraction (XRD) patterns of samples were collected on a Philips PW3040/60 X-ray diffractometer using Cu K $\alpha$  radiation with a scanning rate of 0.06 s<sup>-1</sup>. Morphological information was acquired on a Hitachi S-4800 field emission scanning electron microscope (FESEM). Microstructures were analyzed by transmission electron microscopy (TEM; JEM-2100F), high-resolution transmission electron microscopy (HRTEM), and scanning transmission electron microscopy-energy dispersive X-ray spectra (STEM-EDS) elemental mapping. X-ray photoelectron spectra (XPS) were obtained on an ESCALab MKII X-ray photoelectron spectrometer, and all of the binding energies were referenced to the C 1s level at 284.8 eV. UV-visible diffuse reflectance spectra (UV-vis DRS) were collected on a Thermo Nicolet Evolution 500 UV-vis spectrophotometer. The photoluminescence (PL) and transient photoluminescence spectra (TRPL) were measured by using an excitation wavelength of 375 nm on an FLS 920 and FLS 980 fluorescence spectrophotometer, respectively. The surface photocurrent (SPC) measurements were carried out at room temperature on a surface photovoltage spectrometer (PL-SPV/IPCE1000, Beijing Perfectlight Technology Co., Ltd.) consisting of a source of monochromatic light with a mechanical chopper (SR 540, Stanford research, Inc.). Zeta potentials were assessed by dynamic light-scattering analysis using the Zetasizer Nano ZS90. A Bruker EMX-plus X-band spectrometer was used to acquire the electron paramagnetic resonance (EPR) signals of radical spin-trapped by spin trap reagent 5, 5-dimethyl-1-pyrroline-N-oxide (DMPO) (purchased from Sigma Chemical Co.). In-situ diffuse reflectance infrared Fourier transform spectra (DRIFTS) were acquired on a Bruker INVENIO Fourier-transform infrared spectrometer (Karlsruhe, Germany), equipped with a liquid nitrogen-cooled HgCdTe (MCT) detector. Before the adsorption/desorption process, the samples were purged with He (50 mL min<sup>-1</sup>) for 1 h at 120 °C, then the mixed gas flow (25 mL min<sup>-1</sup> of He and 5 mL min<sup>-1</sup> of CO<sub>2</sub> with a trace of H<sub>2</sub>O vapor) was introduced into the reactor to record the dynamic Fourier transform infrared

spectroscopy (FTIR) signals. After reaching the adsorption equilibrium (~30 min), the background spectrum was collected. Then, turn on the light irradiation (300 W Xe lamp, AM 1.5 filter) and record the FTIR spectra at an interval to investigate the conversion dynamics of reactants under irradiation. The nitrogen adsorption-desorption isotherms of samples were measured at 77 K with Quantachrome autosorb iQ, the USA. The CO<sub>2</sub> adsorption isotherms were measured using a BSD-PS (M) apparatus at 298 K.

## 2.3. Photocatalytic performance tests

Photocatalytic CO<sub>2</sub>RR was performed on an automatic photocatalytic reaction system (Labsolar-6A, Beijing Perfectlight) using a Xe lamp (Microsolar 300, Beijing Perfectlight) with a 420 nm cut-on filter as the visible-light source. Before photocatalytic tests, the as-prepared photocatalyst (15 mg) was dispersed in 2 mL of distilled water and ultrasound for several minutes to form a homogeneous mixture, which was then slowly dropped on a fiberglass paper with an area of 12.56 cm<sup>2</sup> and naturally dried at room temperature. Subsequently, the fiberglass paper was put in a glass vessel (a volume of 380 mL) containing 5 mL of deionized water. After that, the vessel was sealed with a quartz glass top, degassed to remove air, and filled with high-purity CO<sub>2</sub> (99.999%). The temperature of the entire reaction system was kept at 25 °C by cyclic condensed water. The generated gas from the reactor was analyzed by an online gas chromatograph (Shimadzu Gas Chromatograph GC-2014, Ar carrier). Isotope-labeling experiments were conducted under identical test conditions except using <sup>13</sup>CO<sub>2</sub> instead of <sup>12</sup>CO<sub>2</sub>. 0.1 mL of the gas product was withdrawn using a gas-tight syringe for gas analysis. The Agilent Technologies 6890 N network GC system combined with an Agilent Technologies 5975B inert XL MSD model mass spectrometer (GC-MS) was employed to collect the mass spectrometry data. The apparent quantum efficiency (AQE) of S-scheme photocatalytic CO evolution was calculated using the following equation:

$$\text{AQE} = \frac{\text{the number of reacted electrons}}{\text{the number of incident photons}} \times 100\% = \frac{4n_{\text{CO}}N_{\text{A}}h\nu}{WAt} \times 100\% \quad (1)$$

Where  $n_{\text{CO}}$  represents the mole number of evolved CO;  $N_{\text{A}}$  is the Avogadro constant;  $h$  is the Planck constant;  $\nu$ ,  $W$ ,  $A$ , and  $t$  are the incident light frequency, intensity, irradiation area, and time, respectively.

## 2.4. (Photo)electrochemical measurements

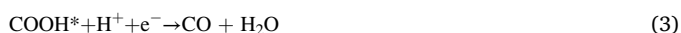
The Mott-Schottky experiment was conducted on Zennium electrochemical workstation (ZAHNER, Germany) with a standard three-electrode system, where Hg/HgO (saturated NaOH) and Pt wire were utilized as reference and counter electrode, respectively. The photocatalyst-coated glassy carbon electrode was used as the working electrode with 0.5 M Na<sub>2</sub>SO<sub>4</sub> aqueous solution as electrolyte. Electrochemical impedance spectroscopy (EIS) measurement was carried out in the three-electrode system by applying an ac voltage of 10 mV with frequency ranging from 0.1 Hz to 100 KHz and the aqueous solutions of K<sub>3</sub>[Fe(CN)<sub>6</sub>] (5 mM) and KCl (1 M) as electrolyte. The photocurrent measurement was performed on an electrochemical station (CHI 660E, China), the procedure was similar to the EIS measurement except using photocatalyst-coated fluorine-doped tin oxide (FTO) glass as a working electrode. The working electrode was prepared by dropping 8  $\mu$ L of photocatalyst-containing suspension (5 mg of photocatalyst powders was dispersed in a mixture of ethylene glycol (30  $\mu$ L), ethanol (50  $\mu$ L), and Nafion (10  $\mu$ L)) on the surface of FTO with 1.5  $\times$  1 cm<sup>2</sup> areas, and dried at 50 °C in an oven.

## 2.5. Density functional theory (DFT) calculations

Periodic DFT-based method with Perdew-Burke-Ernzerh of

functional was applied for all of the calculations in this study using the Vienna ab initio simulation package [43–47]. During the calculations the valence electrons for V, In, O, C, and N atoms were set to  $p^6d^4s^1$ ,  $s^2p^1$ ,  $s^2p^4$ ,  $s^2p^2$ ,  $s^2p^3$ , respectively. The DFT calculations were performed for the crystals, with a cutoff energy of 500 eV. The k-point Monkhorst-Pack grid of  $9 \times 6 \times 8$  was applied for the calculation of the bulk, giving rise to lattice parameters of  $a = 5.81$ ,  $b = 8.58$ , and  $c = 6.68$  Å, in good agreement with experiments [38]. Then, a supercell of  $2 \times 1 \times 1$  was applied for the calculations of the electronic properties of  $\text{InVO}_4$  material. Two different Vo were considered for the  $\text{InVO}_4$  to evaluate the effect of Vo on electronic structures. For the density of states (DOS) calculations, the k-point grid was set to  $9 \times 12 \times 15$ . The optimization of the  $2 \times 2$  unit cells for the buckled  $\text{C}_3\text{N}_4$  was performed using a k-point of  $3 \times 3 \times 1$ , which was increased to  $8 \times 8 \times 1$  for the DOS calculations. The optimized lattice parameters for the buckled  $\text{C}_3\text{N}_4$  are  $a = b = 6.93$  Å, well agreement with the previous DFT calculations [48]. The vacuum was set to 20 Å for the  $\text{C}_3\text{N}_4$  calculations.

To understand the effect of protonation of  $\text{C}_3\text{N}_4$  on  $\text{CO}_2$  hydrogenation, two hydrogen atoms were added to the  $\text{C}_3\text{N}_4$  sheet and the most stable structure was denoted as pristine  $\text{C}_3\text{N}_4$ . Gibbs free energy was calculated for each state in the reaction pathways of  $\text{CO}_2$  hydrogenation using pristine  $\text{C}_3\text{N}_4$  and p- $\text{C}_3\text{N}_4$  models. The key elementary reaction steps for  $\text{CO}_2$  hydrogenation on the two models are given by:



### 3. Results and discussion

The synthetic process of the p- $\text{C}_3\text{N}_4/\text{InVO}_4$  photocatalysts is illustrated in Scheme 1. Firstly, ultrathin  $\text{C}_3\text{N}_4$  nanosheets are prepared according to an intercalation and calcination method [41]. Then,  $\text{In}^{3+}$  and  $\text{VO}_3^-$  ions are sequentially adsorbed on  $\text{C}_3\text{N}_4$  nanosheets with the presence of  $\text{HNO}_3$ , forming p- $\text{C}_3\text{N}_4/\text{InVO}_4$  precursors. Finally, the precursors are hydrothermally treated to obtain the p- $\text{C}_3\text{N}_4/\text{InVO}_4$  hetero-nanosheets.

#### 3.1. Characteristics of the p- $\text{C}_3\text{N}_4/\text{InVO}_4$ hetero-nanosheets

##### 3.1.1. Phase constitution

Phase constitutions of the as-prepared p- $\text{C}_3\text{N}_4$ ,  $\text{InVO}_4$ , and p- $\text{C}_3\text{N}_4/\text{InVO}_4$  with different p- $\text{C}_3\text{N}_4$  content are analyzed by XRD. As shown in Fig. 1a, p- $\text{C}_3\text{N}_4$  only represents a characteristic peak located at  $27.7^\circ$ , corresponding to the diffraction of (002) crystal planes [49,50]. The deletion of a diffraction peak at  $13.1^\circ$  from (100) planes is ascribed to fewer layer number of as-prepared p- $\text{C}_3\text{N}_4$  as well as lattice distortion

resulting from porous structures in-plane units [51]. For pure  $\text{InVO}_4$ , all diffraction peaks are well consistent with the orthorhombic phase (JCPDS No. 71–1689) [39]. A local enlargement of the XRD patterns in the range of  $24\text{--}29^\circ$  shows that all the p- $\text{C}_3\text{N}_4/\text{InVO}_4$  samples contain two sets of diffraction patterns from  $\text{InVO}_4$  and p- $\text{C}_3\text{N}_4$ , and no additional diffraction peaks are observed (Fig. 1b). As the amount of p- $\text{C}_3\text{N}_4$  increases, the diffraction intensity of the (002) plane in p- $\text{C}_3\text{N}_4$  rises. That is,  $\text{InVO}_4$  and p- $\text{C}_3\text{N}_4$  with controllable relative ratios are well combined together, implying the successful fabrication of p- $\text{C}_3\text{N}_4/\text{InVO}_4$  heterojunctions.

##### 3.1.2. Morphology, microstructures, and $\text{CO}_2$ adsorption capacity

FESEM is employed to inspect the morphology and microstructure of samples. As seen from Fig. S1a and b, the as-prepared p- $\text{C}_3\text{N}_4$  shows a representative sheet-like morphology with a smooth surface, and abundant hole structures were formed within nanosheets, which may result from gas releasing ( $\text{CO}_2$ ,  $\text{H}_2\text{O}$ , and  $\text{NH}_3$ ) during the pyrolysis process of  $\text{C}_3\text{N}_4$  precursors [52]. In contrast, pure  $\text{InVO}_4$  appears irregular aggregates with a large size of several micrometers (Fig. S1c and d). After being deposited on p- $\text{C}_3\text{N}_4$  nanosheets, the formed  $\text{InVO}_4$  emerges as cross-linking nano-bundles (Fig. S2a and b). As  $\text{C}_3\text{N}_4$  content increases, these nano-bundles become remarkable, wrapping on the p- $\text{C}_3\text{N}_4$  nanosheets (Fig. 2a and Fig. S2c–f). Note that, such hybrids cannot be formed without the presence of dilute  $\text{HNO}_3$  (Fig. S3), indicating that the  $\text{HNO}_3$  participates in and assists the in-situ growth process of  $\text{InVO}_4$  nanobelts on p- $\text{C}_3\text{N}_4$  nanosheets.

Fig. 2b illustrates TEM images of the p- $\text{C}_3\text{N}_4/\text{InVO}_4$ -5 sample, which confirms the belt-like morphology of  $\text{InVO}_4$  loaded on p- $\text{C}_3\text{N}_4$  nanosheets. The enlarged TEM image further reveals that the length of nanobelts is above  $1 \mu\text{m}$  and the width of nanobelts is distributed in  $32\text{--}45 \text{ nm}$  with an average size of about  $38 \text{ nm}$  (Fig. S4). Such face-to-face contact is very beneficial for the separation and transfer of photo-generated charge carriers [53,54]. The SAED pattern verifies the existence of orthorhombic-phase  $\text{InVO}_4$  (Fig. 2c). The HRTEM image, obtained at the interface, reveals close contact between p- $\text{C}_3\text{N}_4$  and  $\text{InVO}_4$  as well as good crystallinity of  $\text{InVO}_4$  nanobelts, which is conducive to electronic interactions between two components (Fig. 2d). Moreover, one set of clear lattice fringe is observed with a space of  $0.202 \text{ nm}$  corresponding to the diffraction of (132) planes of orthorhombic  $\text{InVO}_4$ , while p- $\text{C}_3\text{N}_4$  appears an amorphous state with no lattice fringes detected [55]. The STEM-EDS elemental mapping (Fig. S5a–f) further confirms the coexistence and uniform distribution of In, V, O, C, and N elements in the p- $\text{C}_3\text{N}_4/\text{InVO}_4$  hetero-nanosheets. These results together demonstrate the successful construction of p- $\text{C}_3\text{N}_4/\text{InVO}_4$  hetero-nanosheets.

To inspect the specific surface area and pore structures of the p- $\text{C}_3\text{N}_4/\text{InVO}_4$  samples, the  $\text{N}_2$  adsorption–desorption isotherms are measured and shown in Fig. S6a–e, and the corresponding pore structural data are listed in Table S1. It can be found that bare  $\text{InVO}_4$  has a very low BET surface area of about  $7 \text{ m}^2 \text{ g}^{-1}$ , while bare p- $\text{C}_3\text{N}_4$  has the highest BET surface area of  $34 \text{ m}^2 \text{ g}^{-1}$  due to abundant porous structures. After being loaded with  $\text{InVO}_4$ , the BET surface area of various p- $\text{C}_3\text{N}_4/\text{InVO}_4$  samples is significantly reduced to a relatively narrow range of  $12 \sim 18 \text{ m}^2 \text{ g}^{-1}$ , due to the covering of porous structures by  $\text{InVO}_4$ , acting as a function of the p- $\text{C}_3\text{N}_4$  content. Moreover, all the samples mainly contain mesoporous structures with a close average pore diameter of around  $30 \text{ nm}$ . These results indicate all the p- $\text{C}_3\text{N}_4/\text{InVO}_4$  samples have no obvious difference in BET surface area and pore structures.

Furthermore, the  $\text{CO}_2$  adsorption tests are carried out for the bare p- $\text{C}_3\text{N}_4$ ,  $\text{InVO}_4$ , and different p- $\text{C}_3\text{N}_4/\text{InVO}_4$  samples. The corresponding adsorption curves and absorbing amount are depicted in Fig. S6f and Table S1. Obviously, the p- $\text{C}_3\text{N}_4$  shows better adsorption affinity toward  $\text{CO}_2$  than pure  $\text{InVO}_4$ . After being loaded with  $\text{InVO}_4$ , the adsorption capacity is gradually promoted with increasing p- $\text{C}_3\text{N}_4$  content. In particular, the p- $\text{C}_3\text{N}_4/\text{InVO}_4$ -5 and p- $\text{C}_3\text{N}_4/\text{InVO}_4$ -7 samples display a

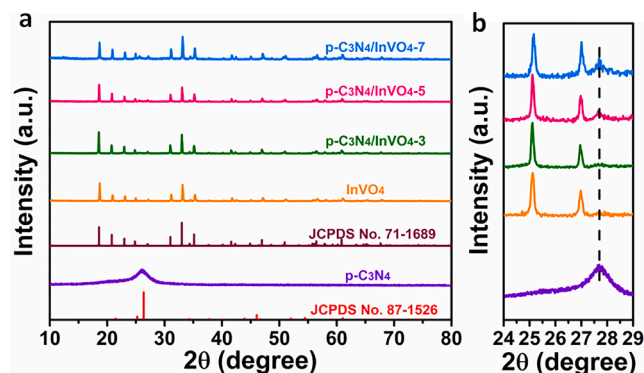


Fig. 1. (a) XRD patterns, and (b) a local enlargement of the XRD patterns in a range of  $24\text{--}29^\circ$  of the as-prepared bare p- $\text{C}_3\text{N}_4$ ,  $\text{InVO}_4$ , and p- $\text{C}_3\text{N}_4/\text{InVO}_4$  with different  $\text{C}_3\text{N}_4$  contents.

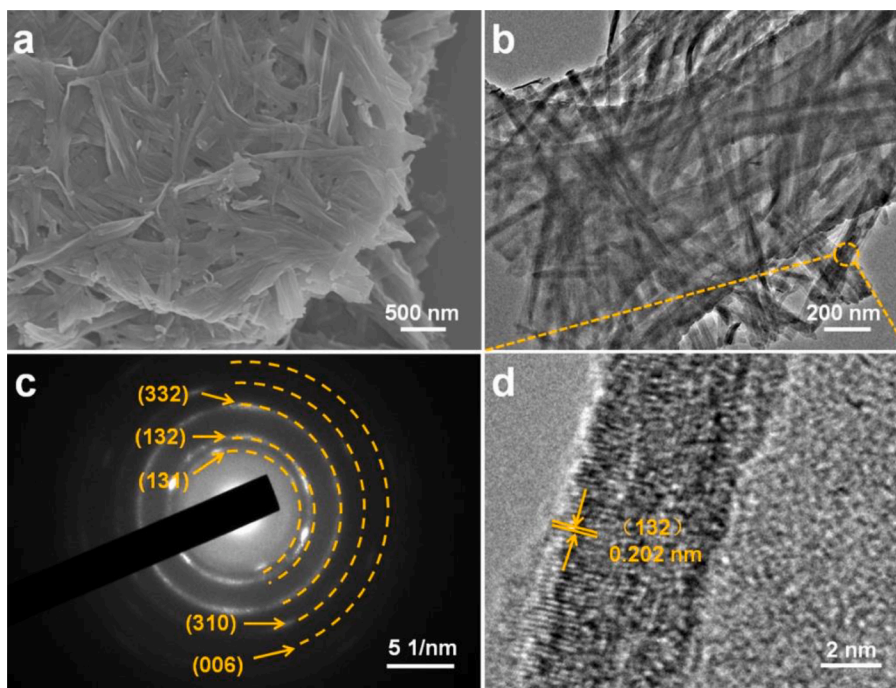


Fig. 2. (a) FESEM, (b) TEM, (c) SAED, and (d) HRTEM images of the p-C<sub>3</sub>N<sub>4</sub>/InVO<sub>4</sub>-5 sample.

close adsorption capacity and outperform other samples, especially the bare InVO<sub>4</sub>. The enhanced CO<sub>2</sub> adsorption is essential for the p-C<sub>3</sub>N<sub>4</sub>/InVO<sub>4</sub> heterostructures to achieve the efficient photocatalysis.

### 3.1.3. Composition and chemical states

The composition and chemical state of samples are further investigated by XPS. The survey XPS spectrum of p-C<sub>3</sub>N<sub>4</sub>/InVO<sub>4</sub>-5 confirms the existence of In, V, O, C, and N elements without impurity elements detected (Fig. S7). To reveal electronic interactions in p-C<sub>3</sub>N<sub>4</sub>/InVO<sub>4</sub>,

the comparison of high-resolution XPS spectra of In 3d, V 2p, and O 1s between bare InVO<sub>4</sub> and p-C<sub>3</sub>N<sub>4</sub>/InVO<sub>4</sub>-5 is made. For bare InVO<sub>4</sub>, the In 3d spectrum depicts two symmetry peaks located at 445.14 and 452.69 eV with splitting energy of 7.55 eV, corresponding to In 3d<sub>5/2</sub> and In 3d<sub>3/2</sub> of In<sup>3+</sup> (Fig. 3a) [56]. The V 2p-binding energies show two doublets: One is located at 517.74 eV and 525.29 eV, corresponding to V 2p<sub>3/2</sub> and V 2p<sub>1/2</sub> of V<sup>5+</sup>, while the other one at 517.05 eV and 523.79 eV are attributed to V 2p<sub>3/2</sub> and V 2p<sub>1/2</sub> of V<sup>3+</sup>, respectively (Fig. 3b) [56]. According to charge neutrality law, the presence of V<sup>3+</sup> probably results

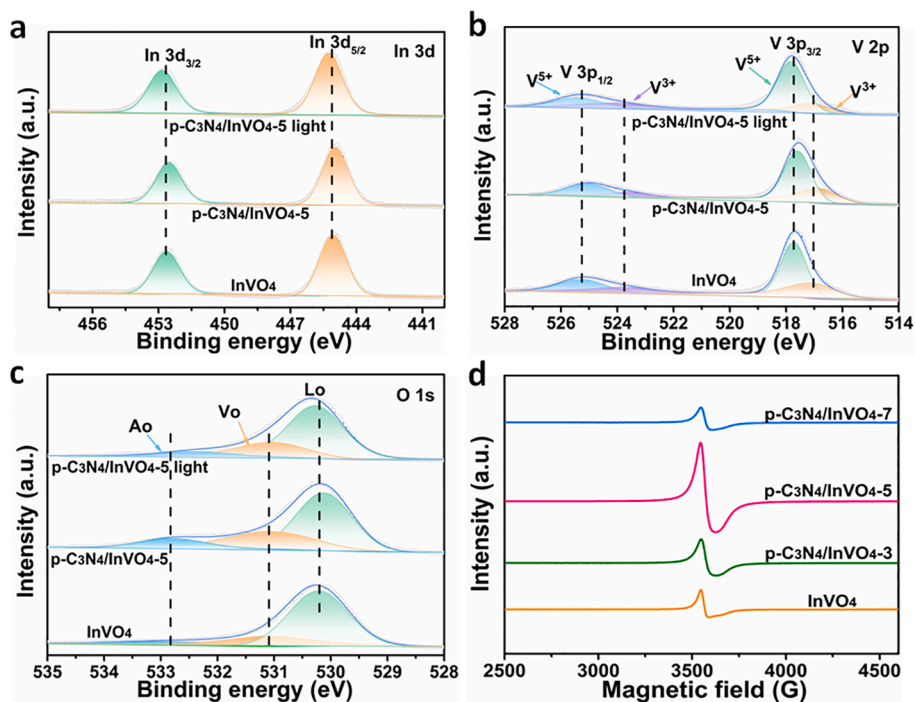


Fig. 3. High-resolution XPS spectra of the bare InVO<sub>4</sub> and p-C<sub>3</sub>N<sub>4</sub>/InVO<sub>4</sub>-5 with and without irradiation: (a) In 3d, (b) V 2p, and (c) O 1s. (d) EPR spectra of the bare InVO<sub>4</sub> and different p-C<sub>3</sub>N<sub>4</sub>/InVO<sub>4</sub> samples.

from the formation of Vo in InVO<sub>4</sub>. As expected, in the O 1s spectrum, besides lattice oxygen (Lo) at 530.20 eV and chemisorbed oxygen (Ao) at 532.60 eV, an evident XPS peak centered at about 531.10 eV is assigned to Vo (Fig. 3c) [57]. The area percentages of Lo, Vo, and Ao are 70.29, 18.79, and 10.92 %, respectively, indicating that a large amount of Vo is formed in bare InVO<sub>4</sub>. The InVO<sub>4</sub>-c displays a silent EPR signal compared to that of the bare InVO<sub>4</sub>, indicating the successful removal of Vo (Fig. S8a). Accordingly, the XPS analysis reveals that no peaks can be fitted at a binding energy of 531.10 eV in the O 1s high-resolution of InVO<sub>4</sub>-c (Fig. S8b), which is in contrast with that of the bare InVO<sub>4</sub> and thus confirm that the peak at 531.10 eV belongs to Vo. For bare InVO<sub>4</sub>, the C 1s spectrum can be fitted into three peaks located at 284.8, 286.2, and 288.7 eV, corresponding to C–C, C–NH<sub>x</sub>, and N–C = N, respectively (Fig. S9). Similarly, the fitted N 1s spectrum also contains three N species: C–N = C, N–(C)<sub>3</sub>, and C–NH at 398.7, 399.7, and 400.9 eV, respectively [41]. Upon hybridization in the p-C<sub>3</sub>N<sub>4</sub>/InVO<sub>4</sub> heterostructure, the XPS peaks of In 3d, V 2p, and O 1s display apparent shifts to lower binding energy, while those of C 1s and N 1s move towards higher binding energy, suggesting electron transfer from p-C<sub>3</sub>N<sub>4</sub> to InVO<sub>4</sub>. Meanwhile, the area percentage of Vo relative to other oxygen species is significantly increased from 18.79 to 29.13 %, indicating that the presence of p-C<sub>3</sub>N<sub>4</sub> is conducive to the formation of Vo in the hybrid process. It is notable that the Vo concentration cannot result in the collapse of InVO<sub>4</sub> since the presence of Vo causes a certain lattice shrinkage, which plays a positive role in the stability of the crystals [58].

### 3.2. Formation mechanism of Vo and roles of dilute HNO<sub>3</sub>

To confirm the presence of Vo and study the influence of p-C<sub>3</sub>N<sub>4</sub> content on the Vo content in hetero-nanosheets, EPR measurements were performed on bare InVO<sub>4</sub> and various p-C<sub>3</sub>N<sub>4</sub>/InVO<sub>4</sub> samples. As expected, bare InVO<sub>4</sub> shows an apparent EPR signal with a g value of 2.003 (Fig. 3d), demonstrating the existence of Vo [59]. Interestingly, the EPR signal intensity in p-C<sub>3</sub>N<sub>4</sub>/InVO<sub>4</sub> varies with the C<sub>3</sub>N<sub>4</sub> content, displaying a volcano-type evolution profile and reaching the maximum on p-C<sub>3</sub>N<sub>4</sub>/InVO<sub>4</sub>-5. It means that the Vo content in p-C<sub>3</sub>N<sub>4</sub>/InVO<sub>4</sub> hetero-nanosheets can be tuned and is up to the highest value in the p-C<sub>3</sub>N<sub>4</sub>/InVO<sub>4</sub>-5 sample.

In the synthetic process of p-C<sub>3</sub>N<sub>4</sub>/InVO<sub>4</sub> hetero-nanosheets, a certain amount of C<sub>3</sub>N<sub>4</sub> and HNO<sub>3</sub> is added. The H<sup>+</sup> is easily adsorbed on the surface of C<sub>3</sub>N<sub>4</sub> through the hydrogen bonding between H<sup>+</sup> and lone pair electrons of the nitrogen, leading to the protonation of C<sub>3</sub>N<sub>4</sub> and electron delocalization in p-C<sub>3</sub>N<sub>4</sub> (Fig. S10a) [60]. The protonation of C<sub>3</sub>N<sub>4</sub> is confirmed by the zeta potential measurements. As shown in Fig. S10b, the zeta potential value of as-prepared C<sub>3</sub>N<sub>4</sub> is –10.3 mV. When treated using HNO<sub>3</sub>, the potential reverses its charge to a positive value (1.44 mV), indicating successful protonation in p-C<sub>3</sub>N<sub>4</sub>.

The formation of Vo in p-C<sub>3</sub>N<sub>4</sub>/InVO<sub>4</sub> can be rationalized from three aspects: (1) Free H<sup>+</sup> from HNO<sub>3</sub> has a strong affinity with lattice oxygen of VO<sub>4</sub><sup>3-</sup> [61], which facilitate the escape of lattice oxygen and thus is beneficial for the Vo formation. (2) The introduction of C<sub>3</sub>N<sub>4</sub> into reaction systems decreases the free H<sup>+</sup> concentration due to the protonation of C<sub>3</sub>N<sub>4</sub> (p-C<sub>3</sub>N<sub>4</sub>), which is somewhat detrimental to the Vo formation. (3) VO<sub>4</sub><sup>3-</sup> can be adsorbed to C<sub>3</sub>N<sub>4</sub>'s surface through the coordination bonds between V 3d empty orbitals and lone pair electrons of nitrogen. The delocalized electrons in p-C<sub>3</sub>N<sub>4</sub> can transfer to the empty orbitals of V<sup>5+</sup>, as evidenced by the XPS analysis (Fig. 3b), which increases the electron density around V<sup>5+</sup> and thus accelerate the dissolution of Lo in an acidic medium. That is, the introduction of C<sub>3</sub>N<sub>4</sub> also has a positive role in the formation of Vo. In a word, the presence of C<sub>3</sub>N<sub>4</sub> in reaction systems gives rise to two opposite effects on the formation of Vo. Note that, for the synthesis of bare InVO<sub>4</sub>, the absence of HNO<sub>3</sub> results in a negligible Vo concentration in the InVO<sub>4</sub>-o sample (Fig. S11). The obtained Vo concentration in the bare InVO<sub>4</sub> with the presence of HNO<sub>3</sub> is higher than that of the g-C<sub>3</sub>N<sub>4</sub>/InVO<sub>4</sub>-5, indicating H<sup>+</sup> has a more remarkable effect on Vo formation than C<sub>3</sub>N<sub>4</sub>.

Based on the above result and analysis, a plausible mechanism of Vo evolution with the C<sub>3</sub>N<sub>4</sub> amount may be described as follows. The HNO<sub>3</sub> concentration in the reaction systems is fixed (5.3 M), as the C<sub>3</sub>N<sub>4</sub> increases, the free H<sup>+</sup> concentration is gradually reduced due to the protonation process but still enough high to create a lot of Vo on the surface of InVO<sub>4</sub> (the total additional amount of C<sub>3</sub>N<sub>4</sub> is still small). At this stage, the negative effect of C<sub>3</sub>N<sub>4</sub> on Vo formation can be neglected, and the positive effect emerges. As a result, the Vo concentration gradually increases with increasing C<sub>3</sub>N<sub>4</sub> (from p-C<sub>3</sub>N<sub>4</sub>/InVO<sub>4</sub>-3 to p-C<sub>3</sub>N<sub>4</sub>/InVO<sub>4</sub>-5), as shown in Fig. 3d. Whereas, when the amount of C<sub>3</sub>N<sub>4</sub> exceeds a critical value and more H<sup>+</sup> ions are used to protonation, resulting in that the free H<sup>+</sup> concentration is insufficient to the formation of Vo. Thus, a reduced Vo concentration can be observed for the p-C<sub>3</sub>N<sub>4</sub>/InVO<sub>4</sub>-7 sample.

Taken together with the above analysis, the dilute HNO<sub>3</sub> is found to play three roles in the synthetic process of the p-C<sub>3</sub>N<sub>4</sub>/InVO<sub>4</sub> hetero-nanosheets as follows: (i) providing H<sup>+</sup> for the protonation process of p-C<sub>3</sub>N<sub>4</sub>, (ii) assisting the in-situ growth of InVO<sub>4</sub> nanobelts on p-C<sub>3</sub>N<sub>4</sub> nanosheets, (iii) facilitating the escape of Lo in VO<sub>4</sub><sup>3-</sup> and thus the formation of Vo in InVO<sub>4</sub>. Hence, the dilute HNO<sub>3</sub> is indispensable for the construction of p-C<sub>3</sub>N<sub>4</sub>/InVO<sub>4</sub> hetero-nanosheets with tunable Vo.

### 3.3. Photocatalytic CO<sub>2</sub> reduction with H<sub>2</sub>O

Photocatalytic CO<sub>2</sub>RR performance of bare InVO<sub>4</sub>, C<sub>3</sub>N<sub>4</sub>, p-C<sub>3</sub>N<sub>4</sub>, and various p-C<sub>3</sub>N<sub>4</sub>/InVO<sub>4</sub> hetero-nanosheets is assessed using a gas–solid reaction model under visible-light irradiation ( $\lambda > 420$  nm). As illustrated in Fig. 4a and b, Both CO and CH<sub>4</sub> can be steadily evolved on all the samples, and CO is the main product. The p-C<sub>3</sub>N<sub>4</sub> exhibits a significantly enhanced catalytic activity compared with C<sub>3</sub>N<sub>4</sub> (C<sub>1</sub> compound production rate: 5.43 vs. 4.29  $\mu\text{mol g}^{-1} \text{h}^{-1}$ ), demonstrating the positive effect of protonation on photocatalytic activity of C<sub>3</sub>N<sub>4</sub>. As expected, bare InVO<sub>4</sub> shows the lowest photocatalytic activity due to the fast recombination of photogenerated carriers and insufficient active sites. When loaded on p-C<sub>3</sub>N<sub>4</sub>, the photocatalytic activity is greatly enhanced on p-C<sub>3</sub>N<sub>4</sub>/InVO<sub>4</sub> hetero-nanosheets. The increase of C<sub>3</sub>N<sub>4</sub> content results in a volcano-like evolution profile of photocatalytic activity among p-C<sub>3</sub>N<sub>4</sub>/InVO<sub>4</sub> samples (Fig. 4c). The p-C<sub>3</sub>N<sub>4</sub>/InVO<sub>4</sub>-5 with the highest V<sub>O</sub> content yields the highest C<sub>1</sub> compound evolution rate of 15.93 (CO: 14.05 and CH<sub>4</sub>: 1.88)  $\mu\text{mol g}^{-1} \text{h}^{-1}$ , 5.93- and 2.93-fold higher than that of bare InVO<sub>4</sub> and p-C<sub>3</sub>N<sub>4</sub>, respectively. In particular, the CO evolution rate is respectively increased by 6.03- and 3.23-times and the selectivity of CO reaches 88%. For the p-C<sub>3</sub>N<sub>4</sub>/InVO<sub>4</sub>-5, the AQE is 0.1% at 420 nm (Fig. S12). The photocatalytic CO<sub>2</sub>RR activity of p-C<sub>3</sub>N<sub>4</sub>/InVO<sub>4</sub>-5 is comparable to those of most C<sub>3</sub>N<sub>4</sub>-based photocatalysts (Table S2). In addition, the excess C<sub>3</sub>N<sub>4</sub> is detrimental to the photocatalytic activity (p-C<sub>3</sub>N<sub>4</sub>/InVO<sub>4</sub>-7), since both Vo content and light absorption capability of InVO<sub>4</sub> would decline.

Furthermore, the photocatalytic activity on p-C<sub>3</sub>N<sub>4</sub>/InVO<sub>4</sub>-5 is enough stable in five cycles of a total of 20 h (Fig. 4d). After cycle tests, there is no significant change in morphology and phase constitution observed for p-C<sub>3</sub>N<sub>4</sub>/InVO<sub>4</sub>-5 (Fig. S13). To determine the origins of CO<sub>2</sub> photoreduction products, we have traced the carbon sources in the reaction using a <sup>13</sup>C isotopic label. As shown in Fig. S14, the major mass spectrum signals with *m/z* values of 29 (<sup>13</sup>CO) and 17 (<sup>13</sup>CH<sub>4</sub>) are clearly observed, indicating that the detected CO and CH<sub>4</sub> indeed originate from the photocatalytic CO<sub>2</sub>RR.

As compared, the photocatalytic activity of the mechanically mixed composite of p-C<sub>3</sub>N<sub>4</sub> and InVO<sub>4</sub> (denoted as p-C<sub>3</sub>N<sub>4</sub> + InVO<sub>4</sub>-5) is also measured and shown in Fig. S15a and b. It can be found that both CO and CH<sub>4</sub> can also be evolved on the p-C<sub>3</sub>N<sub>4</sub> + InVO<sub>4</sub>-5 sample. However, the production rate of the two products is obviously lower than that of the p-C<sub>3</sub>N<sub>4</sub>/InVO<sub>4</sub>-5 photocatalyst. These results indicate that the close contact and interfacial charge transfer in heterostructures are the key factors for enhanced photocatalysis.

Additionally, the O<sub>2</sub> evolution is also detected in the reaction systems

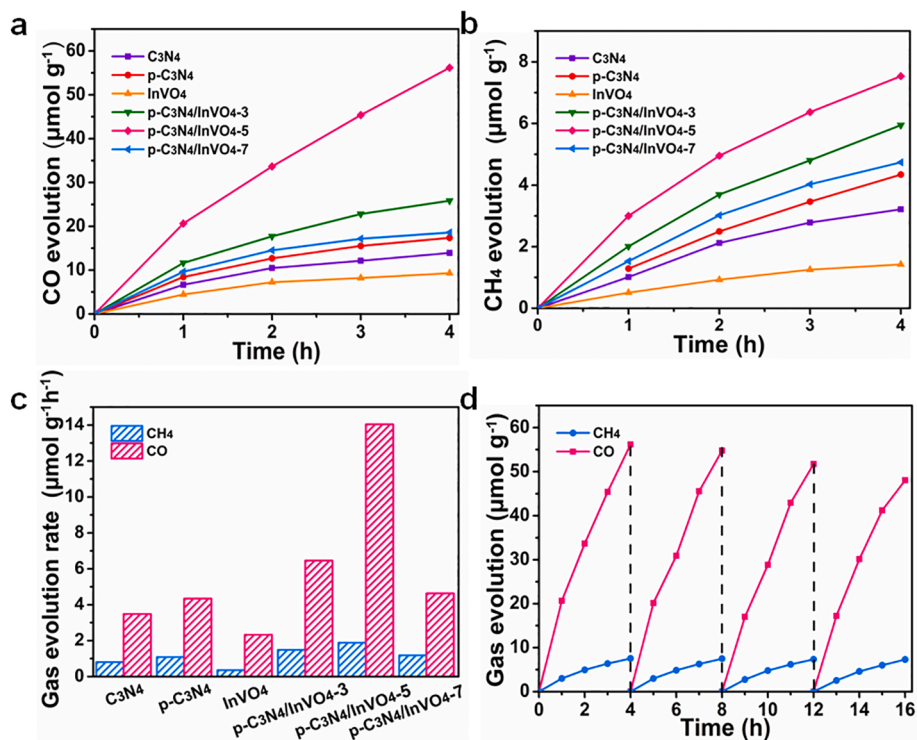


**Fig. 4.** Typical time course of (a) CO and (b) CH<sub>4</sub> production catalyzed by bare C<sub>3</sub>N<sub>4</sub>, p-C<sub>3</sub>N<sub>4</sub>, InVO<sub>4</sub>, and different p-C<sub>3</sub>N<sub>4</sub>/InVO<sub>4</sub> samples. (c) Photocatalytic CO and CH<sub>4</sub> evolution rates on these samples in the first 4 h. (d) Cyclic tests of photocatalytic CO and CH<sub>4</sub> production on the p-C<sub>3</sub>N<sub>4</sub>/InVO<sub>4</sub>-5 sample.

of photocatalytic CO<sub>2</sub>RR. A typical time course of O<sub>2</sub> evolution and corresponding O<sub>2</sub> production rate are displayed in Fig. S16. As it can be seen, O<sub>2</sub> can be evolved on all the bare and hybrid heterostructures. For the p-C<sub>3</sub>N<sub>4</sub>/InVO<sub>4</sub>, the O<sub>2</sub> production rate is 6.52 μmol g<sup>-1</sup> h<sup>-1</sup>, which is about half of the C<sub>1</sub> compounds production rate (15.93 μmol g<sup>-1</sup> h<sup>-1</sup>). The ratio of C<sub>1</sub> and O<sub>2</sub> production rate is relatively close to the theoretical value of 2:1, which indicates that the photogenerated holes participate in the water oxidation reaction for O<sub>2</sub> evolution.

### 3.4. Band structures and transfer mechanism of photogenerated carriers

To investigate the photocatalytic mechanism of p-C<sub>3</sub>N<sub>4</sub>/InVO<sub>4</sub> hetero-nanosheets, the band structures of bare p-C<sub>3</sub>N<sub>4</sub> and InVO<sub>4</sub> are studied by UV-vis DRS and Mott-Schottky plots. As shown in Fig. 5a, the as-prepared C<sub>3</sub>N<sub>4</sub> shows an absorption edge of about 415 nm due to intrinsic band-gap transition. After protonation, the absorption edge of p-C<sub>3</sub>N<sub>4</sub> is extended towards the visible region (about 450 nm), due to the activation of n-π\* transition via protonation [62]. Bare InVO<sub>4</sub> exhibits a further extended absorption edge of about 550 nm with a warped tail in the red-light region, which is an indicator of Vo contained in InVO<sub>4</sub> [63]. Accordingly, all the UV-vis DRSSs of p-C<sub>3</sub>N<sub>4</sub>/InVO<sub>4</sub> hetero-nanosheets appear evidently red-shifted, displaying extended sunlight harvesting, which can be attributed to the hot electron injection caused by the local surface plasmon resonance effect of the rich Vo present on the surface of the hybrid heterojunctions [64]. According to the Tauc equation, the E<sub>g</sub> of p-C<sub>3</sub>N<sub>4</sub> and InVO<sub>4</sub> is determined to be 2.74 and 2.17 eV, respectively (Fig. 5b and c). The Mott-Schottky measurement is performed at three different frequencies (800, 900, and 1000 Hz) to determine the flat band potential (E<sub>fb</sub>) of samples, as shown in Fig. 5d and e. The positive slopes of Mott-Schottky plots indicate the n-type nature of both p-C<sub>3</sub>N<sub>4</sub> and InVO<sub>4</sub>. The E<sub>fb</sub> is derived to be -0.80 and -0.11 eV (vs. NHE, pH = 7) for p-C<sub>3</sub>N<sub>4</sub> and InVO<sub>4</sub>, respectively. Since E<sub>fb</sub> is relatively close to CBM energy (E<sub>CB</sub>) for n-type semiconductors, the E<sub>CB</sub> of p-C<sub>3</sub>N<sub>4</sub> and InVO<sub>4</sub> are determined accordingly [65]. The valence band maximum energy (E<sub>VB</sub>) is calculated from E<sub>CB</sub> + E<sub>g</sub> and determined to be 1.94 eV for p-C<sub>3</sub>N<sub>4</sub> and

2.06 eV for InVO<sub>4</sub>.

Taken together, the band configuration of p-C<sub>3</sub>N<sub>4</sub>/InVO<sub>4</sub> hetero-nanosheets is plotted in Fig. 5f. According to the band alignment, photoexcited electrons have two kinds of transfer routes accessible between two semiconductors, i.e., S-scheme and Type-II routes. When the S-scheme route is adopted, the photoelectrons excited to CB of InVO<sub>4</sub> would be transferred to VB of p-C<sub>3</sub>N<sub>4</sub> to combine with holes, leaving high-energy electrons in CB of p-C<sub>3</sub>N<sub>4</sub> participating in CO<sub>2</sub>RR and holes in VB of InVO<sub>4</sub> for water oxidation reactions. In contrast, if a type-II route is employed, photoelectrons would transfer from CB of p-C<sub>3</sub>N<sub>4</sub> to CB of InVO<sub>4</sub> with lower E<sub>CB</sub> and thus degenerate reduction capacity. Meanwhile, photogenerated holes migrate in the opposite direction between the VB of two semiconductors, also reducing the oxidation ability of holes. Considering that (i) CO is the main reduction product, and (ii) the reduction potential of CO<sub>2</sub>/CO is more negative (-0.53 V) than that of CO<sub>2</sub>/CH<sub>4</sub> (-0.24 V vs. NHE, at pH = 7), being remarkably lower than E<sub>CB</sub> of C<sub>3</sub>N<sub>4</sub> when compared to that of InVO<sub>4</sub>, photoelectrons ought to adopt S-scheme rather than type-II route to reduce CO more easily.

To confirm the charge transfer route in p-C<sub>3</sub>N<sub>4</sub>/InVO<sub>4</sub> under irradiation, radical trapping experiments and EPR analyses were conducted under the assumption that ·O<sub>2</sub><sup>-</sup> and ·OH species are generated only when S-scheme instead of type-II routes are adopted by photoelectrons [66,67]. As depicted in Fig. 6a, the characteristic signals from DMPO/·O<sub>2</sub><sup>-</sup> adducts are clearly observed in methanol suspension of p-C<sub>3</sub>N<sub>4</sub> and p-C<sub>3</sub>N<sub>4</sub>/InVO<sub>4</sub>-5, while no obvious EPR signal is detected in the case of bare InVO<sub>4</sub>, indicating that photoreduction half reaction mainly occurs on the surface of p-C<sub>3</sub>N<sub>4</sub> rather than InVO<sub>4</sub>. The signal intensity of DMPO/·O<sub>2</sub><sup>-</sup> for p-C<sub>3</sub>N<sub>4</sub>/InVO<sub>4</sub>-5 is much higher than that of bare p-C<sub>3</sub>N<sub>4</sub>, suggesting that hetero-nanosheets have higher separation efficiency of photogenerated carriers. On the other hand, the production of ·OH is detected in photocatalyst aqueous suspensions, as shown in Fig. 6b. The EPR signal with an intensity ratio of 1:2:2:1 is detected for InVO<sub>4</sub> and p-C<sub>3</sub>N<sub>4</sub>/InVO<sub>4</sub>-5, whereas no EPR signal is observed for p-C<sub>3</sub>N<sub>4</sub>. Also, the DMPO/·OH signal of p-C<sub>3</sub>N<sub>4</sub>/InVO<sub>4</sub>-5 is higher than that

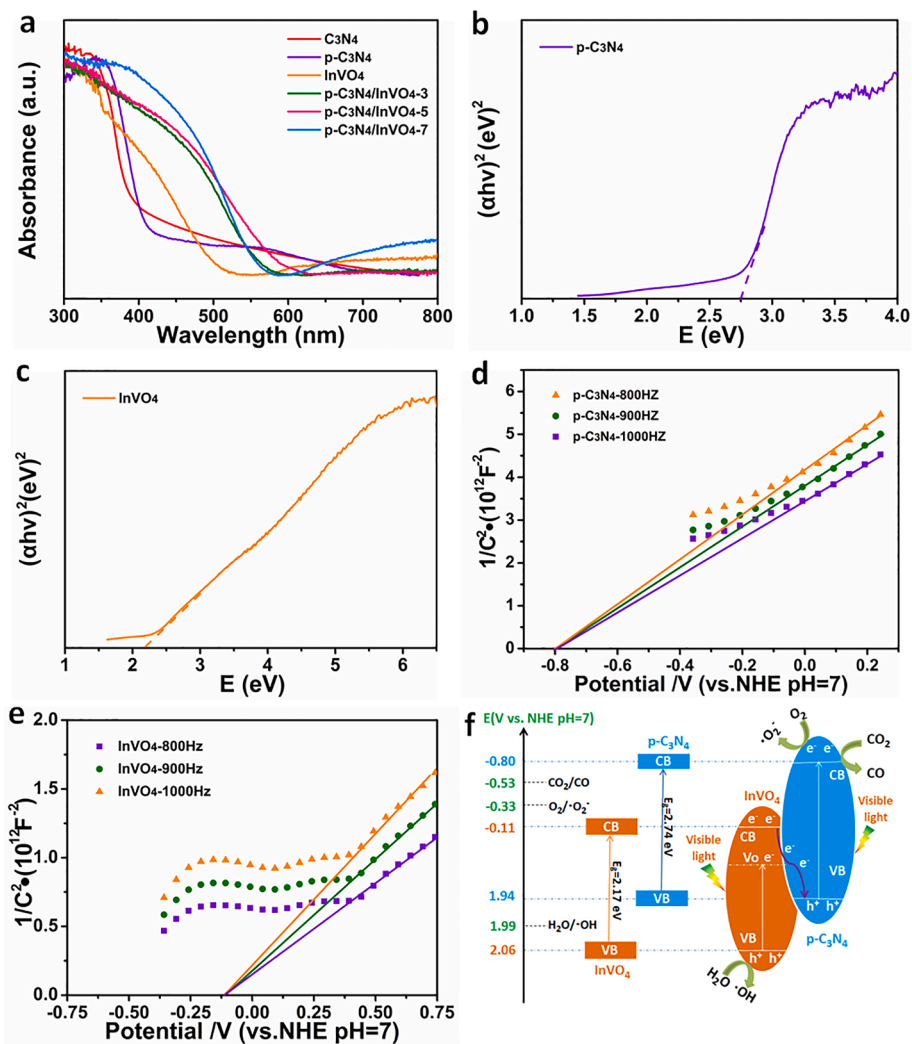


Fig. 5. (a) UV-vis DRS of different samples. Tauc plots of the bare (b) p-C<sub>3</sub>N<sub>4</sub> and (c) InVO<sub>4</sub>. Mott-Schottky plots of the bare (d) p-C<sub>3</sub>N<sub>4</sub> and (e) InVO<sub>4</sub>. (f) Schematic illustration of the band configuration and favored charge transfer pathway in the p-C<sub>3</sub>N<sub>4</sub>/InVO<sub>4</sub> hetero-nanosheets.

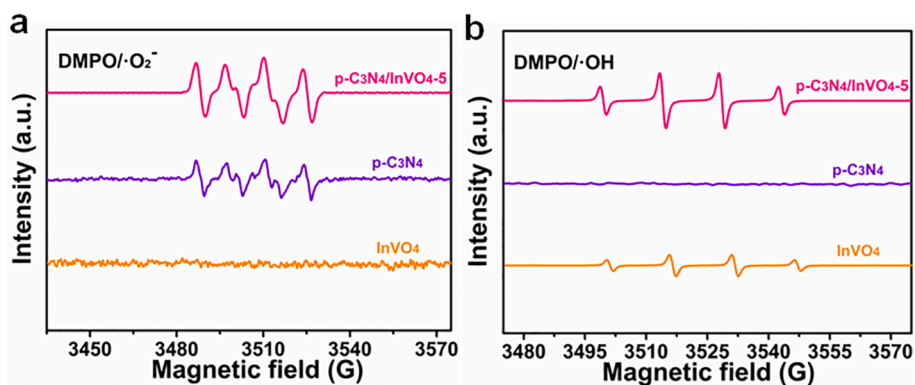


Fig. 6. Identification of dominated free radicals produced in (a) methanol and (b) aqueous suspension of the p-C<sub>3</sub>N<sub>4</sub>/InVO<sub>4</sub>-5, p-C<sub>3</sub>N<sub>4</sub>, and InVO<sub>4</sub> after 5 min of visible-light illumination. EPR results of (a) •O<sub>2</sub><sup>-</sup> and (b) •OH trapped by DMPO.

of pure InVO<sub>4</sub>. That is, the photo-oxidation mostly takes place on InVO<sub>4</sub>. Collectively, the S-scheme route is verified.

To further confirm the S-scheme heterostructures, *in-situ* irradiated XPS measurements were performed on the p-C<sub>3</sub>N<sub>4</sub>/InVO<sub>4</sub>-5 sample. It can be seen that the binding energies of In 3d, V 2p, and O 1s positively shift by about 0.1 eV under visible irradiation relative to those in dark

(Fig. 3a-c). A positive shift of binding energy indicates a decreased electron density around InVO<sub>4</sub>, suggesting the photoelectron transfer direction from InVO<sub>4</sub> to p-C<sub>3</sub>N<sub>4</sub> under light irradiation. Taking the band configuration of the p-C<sub>3</sub>N<sub>4</sub>/InVO<sub>4</sub>-5 into consideration (Fig. 5f), the S-scheme charge transfer pathway is determined [68].

### 3.5. Roles of Vo in photocatalysis

One can see from Fig. 5f that the  $E_{CB}$  of bare  $\text{InVO}_4$  is lower than both reduction potentials of  $\text{CO}_2/\text{CO}$  and  $\text{CO}_2/\text{CH}_4$  (0.53 V and 0.24 eV), the photocatalytic  $\text{CO}_2\text{RR}$  should not be driven in theory. The slight evolution of  $\text{C}_1$  compounds can be rationalized by the presence of Vo as follow. Compared with the perfect surfaces of oxide semiconductors, the Vo is an active site for adsorption and activation of substrate molecules via electron interactions. For the chemisorbed substrate molecule on the Vo of metal oxide semiconductors, the enriched photogenerated electrons around Vo can inject into the antibonding  $\pi$ -orbitals of substrate molecules [69]. Typically, a  $\text{CO}_2$  molecule is fixed by Vo and forms a bond with the sideward transition metal V. Under this condition,  $\text{CO}_2$  molecules donate electrons from their bonding orbitals and accept electrons to their antibonding  $\pi$ -orbitals. Such injection of photogenerated electrons is enhanced by the electrons exchange, which further weakens the C=O bonds and activates  $\text{CO}_2$  molecules [70]. As a result, the photocatalytic  $\text{CO}_2\text{RR}$  still occurs on the surface of the single  $\text{InVO}_4$  with Vo. However, the introduction of excessive Vo in  $\text{InVO}_4$  ( $\text{InVO}_4\text{-r}$ ) is detrimental to the photocatalytic activity, as shown in Fig. S11. The possible reason is that the rich Vo evolves into the recombination centers of photogenerated carriers [71].

The Vo is also expected to enhance the S-scheme photocatalytic efficiency. To this end, the Vo content of p- $\text{C}_3\text{N}_4/\text{InVO}_4\text{-5}$  is significantly reduced via calcination in the air, evidenced by the EPR spectrum

(Fig. S11a), which results in a significant decrement in photocatalytic activity towards  $\text{CO}_2\text{RR}$  in Fig. S11b. This result indicates that Vo attributes to the high photocatalytic activity by enhancing interfacial charge transfer.

To reveal the origin of Vo on enhanced photoactivity, the Vo in  $\text{InVO}_4$  was removed as a comparison by calcining bare  $\text{InVO}_4$  in the air for 4 h, the obtained sample is labeled as  $\text{InVO}_4\text{-c}$ . The Mott-Schottky plots of  $\text{InVO}_4\text{-c}$  are measured as a comparison with bare  $\text{InVO}_4$  (Fig. S17). The corresponding charge carrier density ( $N_D$ ) is calculated according to equation (4): [72]

$$N_D = \left( \frac{2}{e\epsilon\epsilon_0} \right) \left( \frac{d(1/C^2)}{d(E)} \right)^{-1} \quad (4)$$

where  $e$  is the electron charge ( $1.6 \times 10^{-19}$  C),  $\epsilon_0$  is the permittivity of vacuum ( $8.85 \times 10^{-12}$  F  $\text{m}^{-1}$ ),  $\epsilon$  is the dielectric constant of  $\text{InVO}_4$  (50 F  $\text{m}^{-1}$ ),  $C$  represents the space charge capacitance of semiconductors, and  $E$  is the potential applied at the electrode. The  $N_D$  of  $\text{InVO}_4$  with and without Vo is  $9.36 \times 10^{26}$  and  $2.08 \times 10^{27}$   $\text{cm}^{-3}$ , respectively. The great difference in  $N_D$  indicates that the presence of Vo remarkably improves the n-type conductivity of  $\text{InVO}_4$ , which benefits the separation of photogenerated carriers and the S-scheme charge transfer process. Accordingly, the photoelectrical conversion efficiency of the S-scheme system is promoted.

Furthermore, the electronic DOS of  $\text{InVO}_4$  with and without Vo is calculated and shown in Fig. 7. It is found that perfect  $\text{InVO}_4$  without Vo

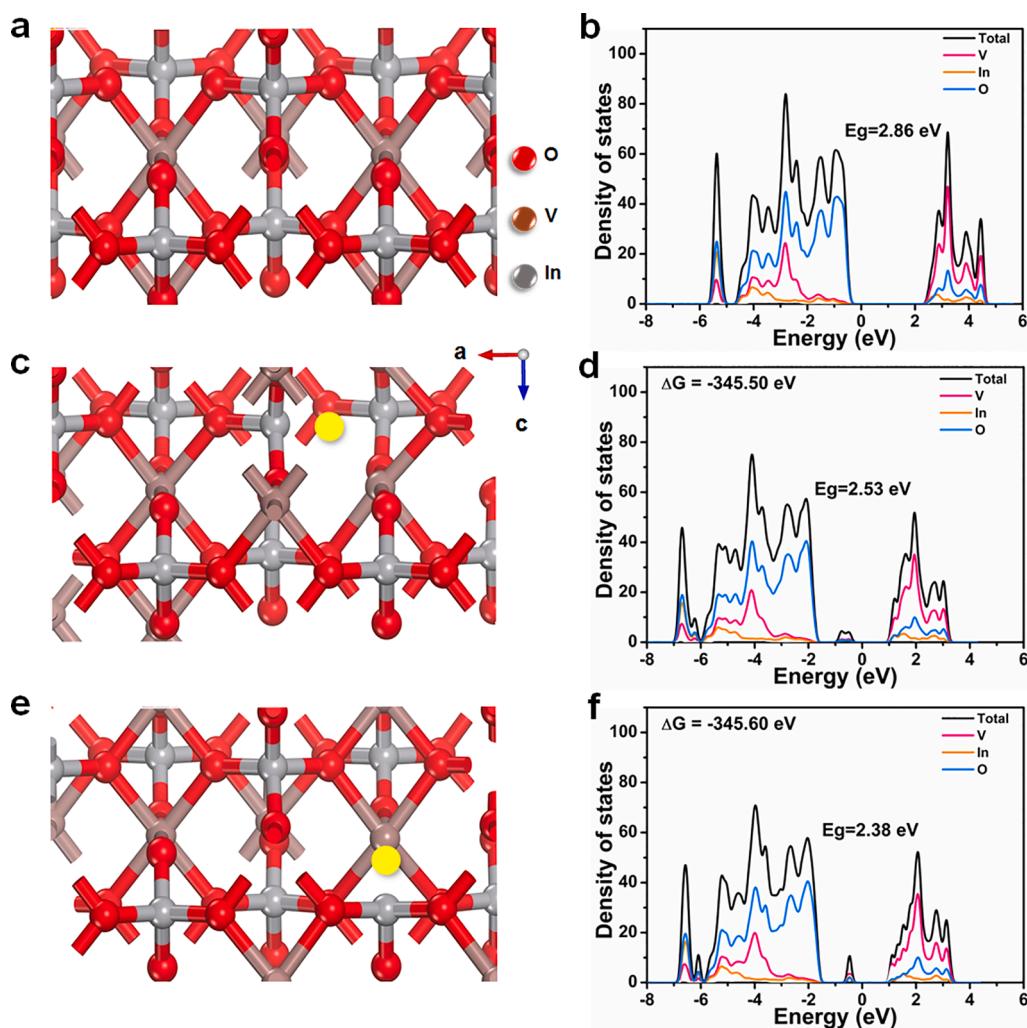


Fig. 7. Crystal structure models and calculated DOS of (a and b) perfect  $\text{InVO}_4$  without Vo, (c and d)  $\text{InVO}_4$  with Vo-1, and (e and f)  $\text{InVO}_4$  with Vo-2. The yellow circles represent Vo. (For interpretation of the references to colour in this figure legend, the reader is referred to the web version of this article.)

has a well-defined band gap between VBM and CBM with a  $E_g$  of 2.86 eV (Fig. 7a and b). When removing one oxygen atom from the perfect model, two kinds of oxygen atoms with different environments could be adopted. The corresponding crystal models are labeled as Vo-1 and Vo-2 (Fig. 7c and e). Note that, the two kinds of Vo-containing models have almost the same formation energy (-345.50 vs. -345.60 eV), indicating they may co-exist in  $\text{InVO}_4$ . The presence of whether Vo-1 or Vo-2 induces the appearance of a new defect state below the Fermi level (Fig. 7d and f), that's the defect state is electron-occupied. As a result, under irradiation, the electrons in defect states can be excited to the CB of  $\text{InVO}_4$ , resulting in significantly reduced  $E_g$  of  $\text{InVO}_4$  and extended visible-light harvesting. Additionally, in the p- $\text{C}_3\text{N}_4/\text{InVO}_4$  the N atom is prone to preferentially adsorb at Vo sites, leading to the close contact of N and V atoms, i.e. the bridging of V-Vo-N. As seen from the DOS profiles of p- $\text{C}_3\text{N}_4$  and  $\text{InVO}_4$ , the CB of  $\text{InVO}_4$  is mostly attributed to the V 3d orbitals (Fig. 7b), while the VB of p- $\text{C}_3\text{N}_4$  is mainly composed of N sp orbitals (Fig. 7e). As such, the bridging of V-Vo-N would promote the combination of electrons in CB of  $\text{InVO}_4$  and holes in VB of p- $\text{C}_3\text{N}_4$ , thus facilitating the charge transfer process in terms of the S-scheme route.

### 3.6. Roles of protonation in photocatalytic $\text{CO}_2\text{RR}$

Next, we investigate the effect of protonation on boosted photocatalytic activity of p- $\text{C}_3\text{N}_4/\text{InVO}_4$  by DFT calculations. As depicted in Fig. 8a-c, there are three kinds of N sites in the framework of  $\text{C}_3\text{N}_4$  accessible for the protonation, which are denoted as  $N_{\text{Aro}}$ ,  $N_{\text{Tet}}$ , and  $N_{\text{Cen}}$ , respectively. It is found that the combination of  $N_{\text{Aro}}$  with proton displays the lowest energy ( $\Delta G = -480.57$  eV), indicating the most stable model of protonation. Hereafter, this model is used to analyze the influence of protonation on the DOS of p- $\text{C}_3\text{N}_4$ . Fig. 8d and e represent the DOS of  $\text{C}_3\text{N}_4$  and p- $\text{C}_3\text{N}_4$ . It is found that protonation lifts the Fermi level of  $\text{C}_3\text{N}_4$ , especially, the entrance of Fermi level into the CB, which is an indicator of quasi-metal. That is, the electrical conductivity of p- $\text{C}_3\text{N}_4$  is greatly promoted, which is conducive to the separation of charge carriers and the electron transfer from p- $\text{C}_3\text{N}_4$  to the adsorbed  $\text{CO}_2$  molecules, thus boosting photocatalytic activity [73].

To gain a deep understanding of the product selectivity, DRIFTS is recorded on the surface of p- $\text{C}_3\text{N}_4/\text{InVO}_4$ -5 with the presence of a certain amount of flowing mixture gas ( $\text{He}/\text{CO}_2$ ) and little  $\text{H}_2\text{O}$ . As shown in Fig. 9, the adsorption equilibrium of  $\text{CO}_2$  on the catalyst surface is reached under flowing mixture gas in dark (0 min). Upon irradiation, multiple reaction intermediates, including  $\text{HCO}_3^-$  (1106, 1187, and  $1453\text{ cm}^{-1}$ ),  $\text{HCOO}^-$  ( $1701\text{ cm}^{-1}$ ), and  $\bullet\text{CO}_2^-$  ( $1294$  and  $1639\text{ cm}^{-1}$ ) are

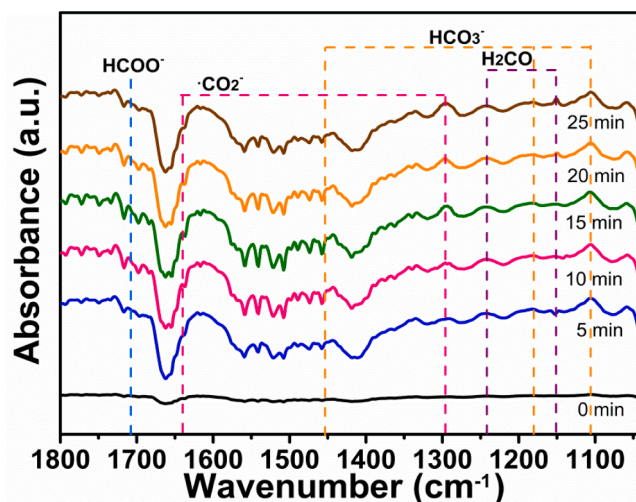


Fig. 9. In-situ DRIFTS spectra of the p- $\text{C}_3\text{N}_4/\text{InVO}_4$ -5 in the mixture gas of He,  $\text{CO}_2$ , and  $\text{H}_2\text{O}$  with and without irradiation.

observed (5 min) [74-78]. The  $\text{HCO}_3^-$  intermediate arises from the surface reaction of adsorbed  $\text{CO}_2$  and  $\text{H}_2\text{O}$ , and the emergence of  $\text{HCOO}^-$  indicates the generation of  $\text{COOH}^*$  [4,74]. As irradiation proceeds, the signal of  $\text{COOH}^*$  is gradually increased up to 20 min and then reduced at 25 min, indicating further transformation. Correspondingly, the signal of  $\bullet\text{CO}_2^-$  species, the main intermediate of  $\text{CO}_2$  to CO [78], is significantly enhanced. Meanwhile, a relatively weak signal corresponding to  $\text{H}_2\text{CO}$  at  $1153$  and  $1248\text{ cm}^{-1}$  is also observed, which corresponds to the intermediate of generating  $\text{CH}_4$  [2]. These observations suggest that the adsorbed  $\text{CO}_2$  molecules are more converted to CO with the generation of little  $\text{CH}_4$ , being consistent with the experimental results.

The DRIFTS analysis reveals that  $\text{COOH}^*$  is the key reaction intermediate formed in photocatalytic  $\text{CO}_2$ -to-CO conversion. Based on this, the reaction thermodynamic and kinetic properties of  $\text{CO}_2$ -to-CO conversion are further studied by DFT calculations, as shown in Fig. 8f. The  $\text{COOH}^*$  formation is the rate-determining step of the whole conversion process, corresponding to a high energy barrier. The energy is reduced by 0.11 eV on p- $\text{C}_3\text{N}_4$  relative to  $\text{C}_3\text{N}_4$ , while the releasing energy of  $\text{COOH}^*$  to  $\text{CO}^*$  increases by 0.25 eV. It means that protonation not only reduces the formation barrier of  $\text{COOH}^*$ , but also facilitates the further conversion of  $\text{COOH}^*$  to  $\text{CO}^*$ , thus promoting whole conversion

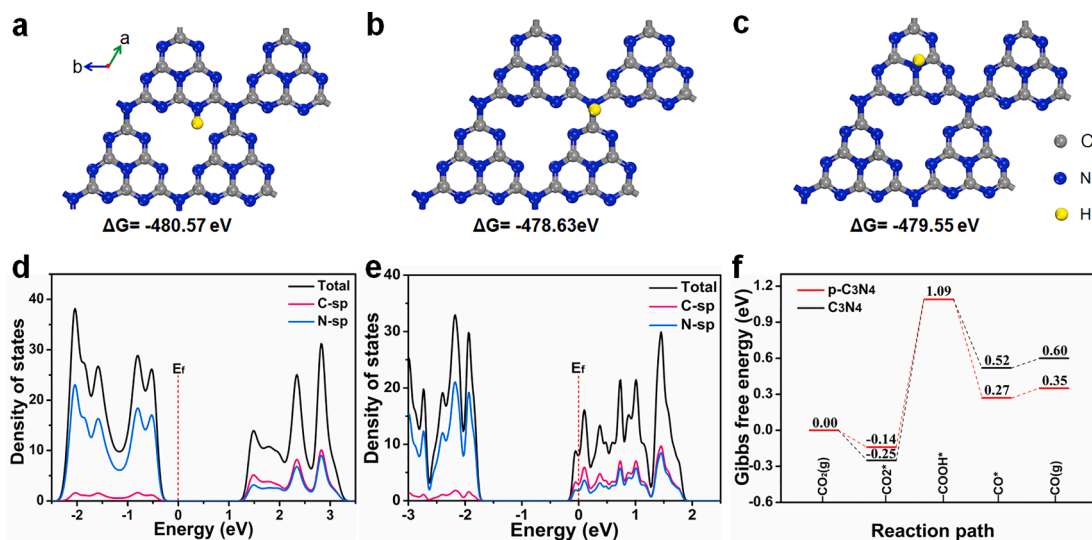


Fig. 8. Crystal structure models of protonated  $\text{C}_3\text{N}_4$  with different N sites: (a)  $N_{\text{Aro}}$  (b)  $N_{\text{Tet}}$ , and (c)  $N_{\text{Cen}}$ . Calculated DOS of the (d)  $\text{C}_3\text{N}_4$  and (e) p- $\text{C}_3\text{N}_4$  nanosheets. (f) Calculated Gibbs free energy for photocatalytic  $\text{CO}_2$  reduction on the p- $\text{C}_3\text{N}_4$  and  $\text{C}_3\text{N}_4$  nanosheets.

efficiency of  $\text{CO}_2$  to CO. To our best knowledge, the effect of protonation on  $\text{CO}_2$  conversion is reported for the first time.

Some control experiments are carried out to support the protonation effects. The  $g\text{-C}_3\text{N}_4/\text{InVO}_4$  composite is prepared by using identical synthetic procedures to the  $p\text{-C}_3\text{N}_4/\text{InVO}_4$  sample except for the presence of dilute  $\text{HNO}_3$ . As shown in Fig. S11a, the EPR measurements reveal that the Vo content of  $g\text{-C}_3\text{N}_4/\text{InVO}_4$  is significantly lower than that of the  $p\text{-C}_3\text{N}_4/\text{InVO}_4$ . Due to the absence of face-to-face interface contact and reduced Vo concentration as well as the non-protonation, the  $g\text{-C}_3\text{N}_4/\text{InVO}_4$  shows a relatively low photocatalytic  $\text{CO}_2\text{RR}$  activity compared with the  $p\text{-C}_3\text{N}_4/\text{InVO}_4$  (Fig. S11b). These results indicate  $\text{HNO}_3$  plays important roles in the construction of the  $p\text{-C}_3\text{N}_4/\text{InVO}_4$  heterostructures for achieving efficient photocatalysis. Besides,  $\text{HNO}_3$  is replaced with  $\text{HCl}$ ,  $\text{H}_2\text{SO}_4$ ,  $\text{H}_3\text{PO}_4$ , and  $\text{HCOOH}$  as protonation resources to synthesis various  $p\text{-C}_3\text{N}_4/\text{InVO}_4$  samples. As shown in Fig. S18, there is no evident difference of photocatalytic  $\text{CO}_2\text{RR}$  activity observed for these samples, indicating that the anions of proton resources have no effects on the photocatalytic activity and the proton plays a key role in constructing  $p\text{-C}_3\text{N}_4/\text{InVO}_4$  heterostructure and efficient  $\text{CO}_2$  photoreduction.

Based on the above analyses, the origin of enhanced photocatalytic  $\text{CO}_2\text{RR}$  activity over  $p\text{-C}_3\text{N}_4/\text{InVO}_4\text{-5}$  is summarized from three aspects as follows. (i) The S-scheme system makes the spatial separation of photogenerated carriers and surface redox sites with high redox potential. (ii) The presence of Vo reduces the  $E_g$  of  $\text{InVO}_4$ , improves the n-type conductivity, and enhances the interfacial coupling between  $\text{InVO}_4$  and  $p\text{-C}_3\text{N}_4$ , thus facilitating the S-scheme photocatalytic efficiency. (iii) The protonation of  $p\text{-C}_3\text{N}_4$  not only increases the electrical conductivity but also promotes the adsorption and activation of  $\text{CO}_2$  molecules as well as the conversion of  $\text{CO}_2$  to CO.

### 3.7. Enhanced charge separation and transfer kinetics

A series of (photo)electrochemical characterizations support the boosted photocatalytic activity by the composite effect of Vo and protonation in the S-scheme system. Fig. 10a illustrates the PL spectra of bare  $\text{InVO}_4$ ,  $\text{C}_3\text{N}_4$ ,  $p\text{-C}_3\text{N}_4$ , and various  $p\text{-C}_3\text{N}_4/\text{InVO}_4$  samples. The as-

prepared  $\text{C}_3\text{N}_4$  shows a strong PL emission, after protonation, the emission is obviously reduced for  $p\text{-C}_3\text{N}_4$ , indicating improved separation of electron-hole pairs by protonation. By contrast, bare  $\text{InVO}_4$  shows a lower PL emission than  $p\text{-C}_3\text{N}_4$ . When loaded on  $p\text{-C}_3\text{N}_4$  ( $p\text{-C}_3\text{N}_4/\text{InVO}_4\text{-3}$ ,  $p\text{-C}_3\text{N}_4/\text{InVO}_4\text{-5}$ , and  $p\text{-C}_3\text{N}_4/\text{InVO}_4\text{-7}$ ), the emission intensity further decreases, suggesting efficient interfacial charge transfer between  $p\text{-C}_3\text{N}_4$  and  $\text{InVO}_4$ . Moreover,  $p\text{-C}_3\text{N}_4/\text{InVO}_4\text{-5}$  with the highest Vo has the lowest PL emission, which is ascribed to the composite effects of Vo and protonation. Accordingly, the  $p\text{-C}_3\text{N}_4/\text{InVO}_4\text{-5}$  has the strongest SPC response than other samples in the irradiation range of 300–450 nm (Fig. 10b). In the wavenumber range, both components can be simultaneously excited to carry out the S-scheme transfer. With visible-light irradiation, the transient photocurrent response of  $p\text{-C}_3\text{N}_4/\text{InVO}_4\text{-5}$  is significantly higher than those of other samples, especially bare  $\text{InVO}_4$ , demonstrating remarkably enhanced photoelectrical efficiency in hetero-nanosheets. Furthermore, the high photocurrent response can be reproduced with light on and declines with light off in each illumination period for five on-off cycles, indicating good stability of the S-scheme transfer process in hetero-nanosheets (Fig. 10c) [79]. The TRPL tests were performed for the  $p\text{-C}_3\text{N}_4$  and  $p\text{-C}_3\text{N}_4/\text{InVO}_4$  samples to confirm the S-scheme electron transfer process. As shown in Fig. S19, the  $p\text{-C}_3\text{N}_4/\text{InVO}_4$  displays a faster fluorescence decline rate than bare  $p\text{-C}_3\text{N}_4$ . By fitting the time-decay fluorescence curves using a double-exponential function, the carrier lifetimes of  $p\text{-C}_3\text{N}_4$  and  $p\text{-C}_3\text{N}_4/\text{InVO}_4$  were determined to be 6.751 and 0.785 ns, respectively. For  $p\text{-C}_3\text{N}_4/\text{InVO}_4$ , the short carrier lifetime results from the effective combination of photo-generated electrons in VB of  $p\text{-C}_3\text{N}_4$  and holes in the CB of  $\text{InVO}_4$ , which indicates the efficient S-scheme charge transfer process in the  $p\text{-C}_3\text{N}_4/\text{InVO}_4$  upon irradiation. Additionally, EIS is measured to evaluate the charge transfer kinetics in hetero-nanosheets [80,81]. As shown in Fig. 10d, the EIS results show that the  $p\text{-C}_3\text{N}_4/\text{InVO}_4\text{-5}$  has a smaller Nyquist radius than other samples, especially bare  $p\text{-C}_3\text{N}_4$  and  $\text{InVO}_4$ . Furthermore, the fitted EIS reveals that the charge transfer resistance ( $R_{ct}$ ) is significantly reduced from  $\text{C}_3\text{N}_4$  to  $p\text{-C}_3\text{N}_4$  (Table S3), supporting the promoted electronic conductivity by protonation. After loading  $\text{InVO}_4$ , the  $R_{ct}$  value is further reduced, varying as the content of  $p\text{-C}_3\text{N}_4$ . It reaches the lowest value on the  $p\text{-C}_3\text{N}_4/\text{InVO}_4\text{-5}$  sample,

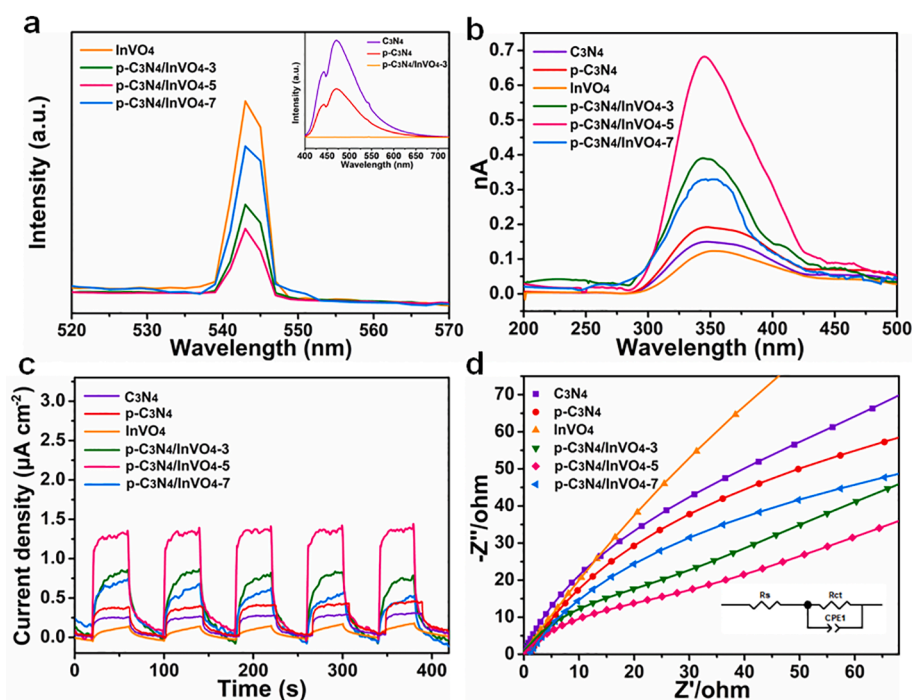


Fig. 10. (a) PL spectra (inset corresponds to the enlarged region in a grey dashed square), (b) SPC in terms of light wavelength, and (c) transient photocurrent response under visible-light irradiation ( $\lambda > 420$  nm) and (d) EIS plots of the bare  $\text{C}_3\text{N}_4$ ,  $p\text{-C}_3\text{N}_4$ ,  $\text{InVO}_4$ , and different  $p\text{-C}_3\text{N}_4/\text{InVO}_4$  samples.

corresponding to the fastest charge transfer kinetics. These results are consistent with the photocatalytic activity of samples.

#### 4. Conclusions

In summary, we have successfully synthesized an S-scheme p-C<sub>3</sub>N<sub>4</sub>/InVO<sub>4</sub> hetero-nanosheet with tunable Vo via in-situ growth of InVO<sub>4</sub> nanobelts on p-C<sub>3</sub>N<sub>4</sub> nanosheets with the assistance of dilute HNO<sub>3</sub> for efficient CO<sub>2</sub> photoconversion. The HNO<sub>3</sub> not only provides H<sup>+</sup> sources for p-C<sub>3</sub>N<sub>4</sub>, but also assists the growth of InVO<sub>4</sub> nanobelts on p-C<sub>3</sub>N<sub>4</sub> and the formation of Vo in InVO<sub>4</sub>. The Vo content is tuned by varying the C<sub>3</sub>N<sub>4</sub> amount, which reduces the free H<sup>+</sup> concentration and increases the electron density around V in VO<sub>4</sub><sup>3-</sup>, leading to a trade-off effect on Vo formation and thus a volcano-shaped evolution profile of Vo content. The optimized p-C<sub>3</sub>N<sub>4</sub>/InVO<sub>4</sub>-5 with abundant Vo possesses the highest photocatalytic CO<sub>2</sub>RR activity, delivering a CO production rate of 14.05 μmol g<sup>-1</sup> h<sup>-1</sup>, which is 6.03 and 3.23 times higher than that of bare InVO<sub>4</sub> and p-C<sub>3</sub>N<sub>4</sub>, respectively. The boosted photocatalytic activity is ascribed to the composite effect of Vo and protonation of C<sub>3</sub>N<sub>4</sub> in the S-scheme system. Vo creates a defect state below the Fermi level, which reduces E<sub>g</sub> for broad visible-light harvesting, enhances the n-type conductivity of InVO<sub>4</sub> and the S-scheme charge transfer. Besides, the protonation of C<sub>3</sub>N<sub>4</sub> not only improves the electrical conductivity for charge transfer to adsorbed CO<sub>2</sub> molecules, but also reduces the formation energy barrier of reaction intermediates of CO<sub>2</sub> to CO. This work provides a new platform for the improvement of photocatalytic activity via integrated engineering of bulk defects and surface catalytic sites.

#### Declaration of Competing Interest

The authors declare that they have no known competing financial interests or personal relationships that could have appeared to influence the work reported in this paper.

#### Acknowledgements

This work is financially supported by the Major Program of Zhejiang Provincial Natural Science Foundation of China (D22B033885), Zhejiang Provincial Ten Thousand Talent Program and the Independent Designing Scientific Research Project of Zhejiang Normal University (2020ZS03). C. Guo acknowledges the financial support from the National Natural Science Foundation of China (22102145).

#### Appendix A. Supplementary data

Supplementary data to this article can be found online at <https://doi.org/10.1016/j.cej.2021.133867>.

#### References

- W. Wang, C. Deng, S. Xie, Y. Li, W. Zhang, H. Sheng, C. Chen, J. Zhao, Photocatalytic C-C coupling from carbon dioxide reduction on copper oxide with mixed-valence Copper(I)/Copper(II), *J. Am. Chem. Soc.* 143 (7) (2021) 2984–2993.
- P. Chen, B. Lei, X. Dong, H. Wang, J. Sheng, W. Cui, J. Li, Y. Sun, Z. Wang, F. Dong, Rare-earth single-atom La-N charge-transfer bridge on Carbon Nitride for highly efficient and selective photocatalytic CO<sub>2</sub> reduction, *ACS Nano* 14 (11) (2020) 15841–15852.
- L. Pei, Y. Yuan, W. Bai, T. Li, H. Zhu, Z. Ma, J. Zhong, S. Yan, Z. Zou, In situ-grown island-shaped hollow Graphene on TaON with spatially separated active sites achieving enhanced visible-light CO<sub>2</sub> reduction, *ACS Catal.* 10 (24) (2020) 15083–15091.
- L. Li, C. Guo, J. Ning, Y. Zhong, D. Chen, Y. Hu, Oxygen-vacancy-assisted construction of FeOOH/CdS heterostructure as an efficient bifunctional photocatalyst for CO<sub>2</sub> conversion and water oxidation, *Appl. Catal. B: Environ.* 293 (15) (2021), 120203.
- H. Wang, W. Ye, Y. Yang, Y. Zhong, Y. Hu, Zn-ion hybrid supercapacitors: Achievements, challenges and future perspectives, *Nano Energy* 85 (2021), 105942.
- Y. Cao, L. Guo, M. Dan, D.E. Doronkin, C. Han, Z. Rao, Y. Liu, J. Meng, Z. Huang, K. Zheng, P. Chen, F. Dong, Y. Zhou, Modulating electron density of vacancy site by single Au atom for effective CO<sub>2</sub> photoreduction, *Nat. Commun.* 12 (1) (2021) 1675.
- J. Li, F. Wei, C. Dong, W. Mu, X. Han, A Z-scheme ZnFe<sub>2</sub>O<sub>4</sub>/RGO/In<sub>2</sub>O<sub>3</sub> hierarchical photocatalyst for efficient CO<sub>2</sub> reduction enhancement, *J. Mater. Chem. A* 8 (14) (2020) 6524–6531.
- Y. Cao, R. Zhang, T. Zhou, S. Jin, J. Huang, L. Ye, Z. Huang, F. Wang, Y. Zhou, B-O bonds in ultrathin Boron Nitride nanosheets to promote photocatalytic carbon dioxide conversion, *ACS Appl. Mater. Interfaces* 12 (8) (2020) 9935–9943.
- T. Inoue, A. Fujishima, S. Konishi, K. Honda, Satoshi, Kenichi, Photoelectrocatalytic reduction of carbon dioxide in aqueous suspensions of semiconductor powders, *Nature* 277 (5698) (1979) 637–638.
- Y. Wang, S. Wang, S.L. Zhang, X.W. Lou, Formation of hierarchical FeCoS<sub>2</sub>-CoS<sub>2</sub> double-shelled nanotubes with enhanced self-performance for photocatalytic reduction of CO<sub>2</sub>, *Angew. Chem. Int. Ed.* 59 (29) (2020) 11918–11922.
- L. Huang, B. Li, B. Su, Z. Xiong, C. Zhang, Y. Hou, Z. Ding, S. Wang, Fabrication of hierarchical Co<sub>3</sub>O<sub>4</sub>@CdIn<sub>2</sub>S<sub>4</sub> p-n heterojunction photocatalysts for improved CO<sub>2</sub> reduction with visible light, *J. Mater. Chem. A* 8 (15) (2020) 7177–7183.
- Q. Mu, W. Zhu, G. Yan, Y. Lian, Y. Yao, Q. Li, Y. Tian, P. Zhang, Z. Deng, Y. Peng, Activity and selectivity regulation through varying the size of cobalt active sites in photocatalytic CO<sub>2</sub> reduction, *J. Mater. Chem. A* 6 (42) (2018) 21110–21119.
- J. Di, C. Zhu, M. Ji, M. Duan, R. Long, C. Yan, K. Gu, J. Xiong, Y. She, J. Xia, H. Li, Z. Liu, Defect-rich Bi<sub>12</sub>O<sub>17</sub>Cl<sub>2</sub> nanotubes self-accelerating charge separation for boosting photocatalytic CO<sub>2</sub> reduction, *Angew. Chem. Int. Ed.* 57 (45) (2018) 14847–14851.
- C. Guo, L. Li, F. Chen, J. Ning, Y. Zhong, Y. Hu, One-step phosphorization preparation of gradient-P-doped CdS/CoP hybrid nanorods having multiple channel charge separation for photocatalytic reduction of water, *J. Colloid Interf. Sci.* 596 (15) (2021) 431–441.
- H. Liu, K. Tian, J. Ning, Y. Zhong, Z. Zhang, Y. Hu, One-step solvothermal formation of Pt nanoparticles decorated Pt<sup>2+</sup>-doped α-Fe<sub>2</sub>O<sub>3</sub> nanoplates with enhanced photocatalytic O<sub>2</sub> evolution, *ACS Catal.* 9 (2) (2019) 1211–1219.
- H.K. Wu, Y.H. Li, M.Y. Qi, Q. Lin, Y.J. Xu, Enhanced photocatalytic CO<sub>2</sub> reduction with suppressing H<sub>2</sub> evolution via Pt cocatalyst and surface SiO<sub>2</sub> coating, *Appl. Catal. B: Environ.* 278 (5) (2020), 119267.
- H. Zhang, C. Guo, J. Ren, J. Ning, Y. Zhong, Z. Zhang, Y. Hu, Beyond CoO<sub>x</sub>: a versatile amorphous cobalt species as an efficient cocatalyst for visible-light-driven photocatalytic water oxidation, *Chem. Commun.* 55 (93) (2019) 14050–14053.
- C. Yang, Q. Tan, Q. Li, J. Zhou, J. Fan, B. Li, J. Sun, K. Lv, 2D/2D Ti<sub>3</sub>C<sub>2</sub> MXene/g-C<sub>3</sub>N<sub>4</sub> nanosheets heterojunction for high efficient CO<sub>2</sub> reduction photocatalyst: Dual effects of urea, *Appl. Catal. B: Environ.* 268 (5) (2020) 118738.
- H. Deng, X. Fei, Y. Yang, J. Fan, J. Yu, B. Cheng, L. Zhang, S-scheme heterojunction based on p-type ZnMn<sub>2</sub>O<sub>4</sub> and n-type ZnO with improved photocatalytic CO<sub>2</sub> reduction activity, *Chem. Eng. J.* 409 (1) (2021), 127377.
- S. Zhao, K. Li, J. Du, C. Song, X. Guo, Facile Construction of a hollow In<sub>2</sub>S<sub>3</sub>/Polymeric carbon nitride heterojunction for efficient visible-light-driven CO<sub>2</sub> reduction, *ACS Sustain. Chem. Eng.* 9 (17) (2021) 5942–5951.
- L. Jiang, X. Yuan, G. Zeng, J. Liang, Z. Wu, H. Wang, Construction of an all-solid-state Z-scheme photocatalyst based on graphite carbon nitride and its enhancement to catalytic activity, *Environ. Sci-Nano* 5 (3) (2018) 599–615.
- Y. Wang, X. Shang, J. Shen, Z. Zhang, D. Wang, J. Lin, J.C.S. Wu, X. Fu, X. Wang, C. Li, Direct and indirect Z-scheme heterostructure-coupled photosystem enabling cooperation of CO<sub>2</sub> reduction and H<sub>2</sub>O oxidation, *Nat. Commun.* 11 (1) (2020) 3043.
- Y. Bai, L. Ye, L. Wang, X. Shi, P. Wang, W. Bai, P.K. Wong, g-C<sub>3</sub>N<sub>4</sub>/Bi<sub>2</sub>O<sub>5</sub>I<sub>2</sub> heterojunction with I<sub>3</sub><sup>-</sup>/I<sup>-</sup> redox mediator for enhanced photocatalytic CO<sub>2</sub> conversion, *Appl. Catal. B: Environ.* 194 (5) (2016) 98–104.
- Y. Miseki, S. Fujiyoshi, T. Gunji, K. Sayama, Photocatalytic water splitting under visible light utilizing I<sub>3</sub><sup>-</sup>/I<sup>-</sup> and IO<sub>3</sub><sup>-</sup>/I<sup>-</sup> redox mediators by Z-scheme system using surface treated PtO<sub>x</sub>/WO<sub>3</sub> as O<sub>2</sub> evolution photocatalyst, *Catal. Sci. Technol.* 3 (7) (2013) 1750, <https://doi.org/10.1039/c3cy00055a>.
- Y. Ji, R. Yang, L. Wang, G. Song, A. Wang, Y. Lv, M. Gao, J. Zhang, X. Yu, Visible light active and noble metal free Nb<sub>4</sub>N<sub>5</sub>/TiO<sub>2</sub> nanobelt surface heterostructure for plasmonic enhanced solar water splitting, *Chem. Eng. J.* 402 (15) (2020), 126226.
- S. Wageh, A.A. AlGhamdi, R. Jafer, X. Li, P. Zhang, A new heterojunction in photocatalysis: S-scheme heterojunction, *Chinese J. Catal.* 42 (5) (2021) 667–669.
- L. Wang, B. Cheng, L. Zhang, J. Yu, In situ irradiated XPS investigation on S-scheme TiO<sub>2</sub>@ZnIn<sub>2</sub>S<sub>4</sub> photocatalyst for efficient photocatalytic CO<sub>2</sub> reduction, *Small* 17 (41) (2021) 2103447.
- Z. Miao, Q. Wang, Y. Zhang, L. Meng, X. Wang, In situ construction of S-scheme AgBr/BiOBr heterojunction with surface oxygen vacancy for boosting photocatalytic CO<sub>2</sub> reduction with H<sub>2</sub>O, *Appl. Catal. B: Environ.* 301 (2022), 120802.
- Y.i. Chen, F. Wang, Y. Cao, F. Zhang, Y. Zou, Z. Huang, L. Ye, Y. Zhou, Interfacial oxygen vacancy engineered two-dimensional g-C<sub>3</sub>N<sub>4</sub>/BiOCl heterostructures with boosted photocatalytic conversion of CO<sub>2</sub>, *ACS Appl. Energy Mater.* 3 (5) (2020) 4610–4618.
- W. Zhao, W. Wang, H. Shi, 2D/2D Z-scheme BiO<sub>1-x</sub>Br/g-C<sub>3</sub>N<sub>4</sub> heterojunction with rich oxygen vacancies as electron mediator for enhanced visible-light degradation activity, *Appl. Surf. Sci.* 528 (30) (2020), 146925.
- Q. Liu, Z. Chen, W. Tao, H. Zhu, L. Zhong, F. Wang, R. Zou, Y. Lei, C. Liu, X. Peng, Edge activation of an inert polymeric carbon nitride matrix with boosted absorption kinetics and near-infrared response for efficient photocatalytic CO<sub>2</sub> reduction, *J. Mater. Chem. A* 8 (23) (2020) 11761–11772.
- Z. Sun, S. Wang, Q. Li, M. Lyu, T. Butburee, B. Luo, H. Wang, J.M.T.A. Fischer, C. Zhang, Z. Wu, L. Wang, Enriching CO<sub>2</sub> activation sites on graphitic carbon

- nitride with simultaneous introduction of electron-transfer promoters for superior photocatalytic CO<sub>2</sub>-to-fuel conversion, *Adv. Sustain. Syst.* 1 (3) (2017) 1700003.
- [33] X. Zhang, X. Zhang, W. Ali, X. Chen, K. Hu, Z. Li, Y. Qu, L. Bai, Y. Gao, L. Jing, Improved photoactivities of large-surface-area g-C<sub>3</sub>N<sub>4</sub> for CO<sub>2</sub> conversion by controllably introducing Co- and Ni-species to effectively modulate photogenerated charges, *ChemCatChem* 11 (24) (2019) 6282–6287.
- [34] C. Ye, J.-X. Li, Z.-J. Li, X.-B. Li, X.-B. Fan, L.-P. Zhang, B. Chen, C.-H. Tung, L.-Z. Wu, Enhanced driving force and charge separation efficiency of protonated g-C<sub>3</sub>N<sub>4</sub> for photocatalytic O<sub>2</sub> evolution, *ACS Catal.* 5 (11) (2015) 6973–6979.
- [35] J. Zhang, M. Zhang, L. Lin, X. Wang, Sol processing of conjugated carbon nitride powders for thin-film fabrication, *Angew. Chem. Int. Ed.* 54 (21) (2015) 6297–6301.
- [36] X. Wang, K. Maeda, A. Thomas, K. Takanebe, G. Xin, J.M. Carlsson, K. Domen, M. Antonietti, A metal-free polymeric photocatalyst for hydrogen production from water under visible light, *Nat. Mater.* 8 (1) (2009) 76–80.
- [37] X. Zhang, J. Zhang, J. Yu, Y. Zhang, F. Yu, L. Jia, Y. Tan, Y. Zhu, B. Hou, Enhancement in the photocatalytic antifouling efficiency over cherimoya-like InVO<sub>4</sub>/BiVO<sub>4</sub> with a new vanadium source, *J. Colloid Interf. Sci.* 533 (1) (2019) 358–368.
- [38] D. Errandonea, O. Gomis, B. Garcia-Domene, J. Pellicer-Porres, V. Katari, S. N. Achary, A.K. Tyagi, C. Popescu, New polymorph of InVO<sub>4</sub>: A high-pressure structure with six-coordinated vanadium, *Inorg. Chem.* 52 (21) (2013) 12790–12798.
- [39] X. Yuan, L. Jiang, J. Liang, Y. Pan, J. Zhang, H. Wang, L. Leng, Z. Wu, R. Guan, G. Zeng, In-situ synthesis of 3D microsphere-like In<sub>2</sub>S<sub>3</sub>/InVO<sub>4</sub> heterojunction with efficient photocatalytic activity for tetracycline degradation under visible light irradiation, *Chem. Eng. J.* 356 (15) (2019) 371–381.
- [40] S. Wang, H. Wang, C. Huang, P. Ye, X. Luo, J. Ning, Y. Zhong, Y. Hu, Trifunctional electrocatalyst of N-doped Graphitic Carbon nanosheets encapsulated with CoFe alloy nanocrystals: The key roles of bimetal components and high-content Graphitic-N, *Appl. Catal. B: Environ.* 298 (5) (2021), 120512.
- [41] Y. Xiao, G. Tian, W. Li, Y. Xie, B. Jiang, C. Tian, D. Zhao, H. Fu, Molecule self-assembly synthesis of porous few-layer Carbon Nitride for highly efficient photoredox catalysis, *J. Am. Chem. Soc.* 141 (6) (2019) 2508–2515.
- [42] X. Wang, X. Li, J. Mu, S. Fan, X. Chen, L. Wang, Z. Yin, M. Tade, S. Liu, Oxygen vacancy-rich porous Co<sub>3</sub>O<sub>4</sub> nanosheets toward boosted NO reduction by CO and CO oxidation: Insights into the structure-activity relationship and performance enhancement mechanism, *ACS Appl. Mater. Interfaces* 11 (45) (2019) 41988–41999.
- [43] J.P. Perdew, K. Burke, M. Ernzerhof, Generalized gradient approximation made simple, *Phys. Rev. Lett.* 78 (18) (1997) 1396.
- [44] G. Kresse, J. Hafner, Ab initio molecular dynamics for liquid metals, *Phys. Rev. B* 47 (1) (1993) 558–561.
- [45] G. Kresse, J. Hafner, Ab initio molecular-dynamics simulation of the liquid-metal-amorphous-semiconductor transition in germanium, *Phys. Rev. B* 49 (20) (1994) 14251–14269.
- [46] G. Kresse, J. Furthmüller, Efficient iterative schemes for Ab initio total-energy calculations using a plane-wave basis set, *Phys. Rev. B* 54 (16) (1996) 11169–11186.
- [47] G. Kresse, J. Furthmüller, Efficiency of Ab-initio total energy calculations for metals and semiconductors using a plane-wave basis set, *Comput. Mater. Sci.* 6 (1) (1996) 15–50.
- [48] H. Niu, X. Wang, C. Shao, Y. Liu, Z. Zhang, Y. Guo, Revealing the oxygen reduction reaction activity origin of single atoms supported on g-C<sub>3</sub>N<sub>4</sub> monolayers: A first-principles study, *J. Mater. Chem. A* 8 (14) (2020) 6555–6563.
- [49] Z. Jiang, W. Wan, H. Li, S. Yuan, H. Zhao, P.K. Wong, A hierarchical Z-scheme α-Fe<sub>2</sub>O<sub>3</sub>/g-C<sub>3</sub>N<sub>4</sub> hybrid for enhanced photocatalytic CO<sub>2</sub> reduction, *Adv. Mater.* 30 (10) (2018) 1706108.
- [50] C. Li, S. Yu, H. Dong, Y. Wang, H. Wu, X. Zhang, G. Chen, C. Liu, Mesoporous ferrihydrite oxide nanoreactors modified on graphitic carbon nitride towards improvement of physical, photoelectrochemical properties and photocatalytic performance, *J. Colloid Interf. Sci.* 531 (1) (2018) 331–342.
- [51] Y. Wang, L. Li, Y. Wei, J. Xue, H. Chen, L.i. Ding, J. Caro, H. Wang, Water transport with ultralow friction through partially exfoliated g-C<sub>3</sub>N<sub>4</sub> nanosheet membranes with self-supporting spacers, *Angew. Chem. Int. Ed.* 56 (31) (2017) 8974–8980.
- [52] W. Tu, Y. Xu, J. Wang, B. Zhang, T. Zhou, S. Yin, S. Wu, C. Li, Y. Huang, Y. Zhou, Z. Zou, J. Robertson, M. Kraft, R. Xu, Investigating the role of tunable nitrogen vacancies in Graphitic Carbon Nitride nanosheets for efficient visible-light-driven H<sub>2</sub> evolution and CO<sub>2</sub> reduction, *ACS Sustain. Chem. Eng.* 5 (8) (2017) 7260–7268.
- [53] Y. Huang, K. Wang, T. Guo, J. Li, X. Wu, G. Zhang, Construction of 2D/2D Bi<sub>2</sub>Se<sub>3</sub>/g-C<sub>3</sub>N<sub>4</sub> nanocomposite with high interfacial charge separation and photo-heat conversion efficiency for selective photocatalytic CO<sub>2</sub> reduction, *Appl. Catal. B: Environ.* 277 (15) (2020), 119232.
- [54] S. She, X. Zhang, X. Wu, J. Li, G. Zhang, The fabrication of two-dimensional g-C<sub>3</sub>N<sub>4</sub>/NaBiO<sub>3</sub>·2H<sub>2</sub>O heterojunction for improved photocatalytic CO<sub>2</sub> reduction: DFT study and mechanism unveiling, *J. Colloid Interface Sci.* 604 (15) (2021) 122–130.
- [55] X. Zhao, Y. Fan, W. Zhang, X. Zhang, D. Han, L.i. Niu, A. Ivaska, Nanoengineering construction of Cu<sub>2</sub>O nanowire arrays encapsulated with g-C<sub>3</sub>N<sub>4</sub> as 3D spatial reticulation All-Solid-State direct Z-scheme photocatalysts for photocatalytic reduction of carbon dioxide, *ACS Catal.* 10 (11) (2020) 6367–6376.
- [56] W. Ding, X. Lin, G. Ma, Q. Lu, Designed formation of InVO<sub>4</sub>/CeVO<sub>4</sub> hollow nanobelts with Z-scheme charge transfer: Synergistically boosting visible-light-driven photocatalytic degradation of tetracycline, *J. Environ. Chem. Eng.* 8 (6) (2020), 104588.
- [57] D. Xu, Y. Liu, Y. Zhang, Z. Shi, M. Yang, C. Zhang, B. Liu, Fabrication of pyramid-BiVO<sub>4</sub>/CdSe composite with controlled surface oxygen vacancies boosting efficient carriers' separation for photocathodic protection, *Chem. Eng. J.* 393 (1) (2020), 124693.
- [58] P. Zeng, Z. Chen, W. Zhou, H. Gu, Z. Shao, S. Liu, Re-evaluation of Ba<sub>0.5</sub>Sr<sub>0.5</sub>Co<sub>0.8</sub>Fe<sub>0.2</sub>O<sub>3-δ</sub> perovskite as oxygen semi-permeable membrane, *J. Membrane Sci.* 291 (1-2) (2007) 148–156.
- [59] Y. Liu, R. Wang, Z. Yang, H. Du, Y. Jiang, C. Shen, K. Liang, A. Xu, Enhanced visible-light photocatalytic activity of Z-scheme graphitic carbon nitride/oxygen vacancy-rich zinc oxide hybrid photocatalysts, *Chinese J. Catal.* 36 (12) (2015) 2135–2144.
- [60] L.i. Shi, K. Chang, H. Zhang, X. Hai, L. Yang, T. Wang, J. Ye, Drastic Enhancement of photocatalytic activities over phosphoric acid protonated porous g-C<sub>3</sub>N<sub>4</sub> nanosheets under visible light, *Small* 12 (32) (2016) 4431–4439.
- [61] D. Yao, C. Dong, Q. Bing, Y.i. Liu, F. Qu, M. Yang, B. Liu, B. Yang, H. Zhang, Oxygen-defective ultrathin BiVO<sub>4</sub> nanosheets for enhanced gas sensing, *ACS Appl. Mater. Interfaces* 11 (26) (2019) 23495–23502.
- [62] D. Wu, S. Hu, H. Xue, X. Hou, H. Du, G. Xu, Y. Yuan, Protonation and microwave-assisted heating induced excitation of lone-pair electrons in Graphitic Carbon Nitride for increased photocatalytic hydrogen generation, *J. Mater. Chem. A* 7 (35) (2019) 20223–20228.
- [63] Z. You, Y. Su, Y. Yu, H. Wang, T. Qin, F. Zhang, Q. Shen, H. Yang, Preparation of g-C<sub>3</sub>N<sub>4</sub> nanorod/InVO<sub>4</sub> hollow sphere composite with enhanced visible-light photocatalytic activities, *Appl. Catal. B: Environ.* 213 (15) (2017) 127–135.
- [64] T. Jia, J. Wu, J. Song, Q. Liu, J. Wang, Y. Qi, P. He, X. Qi, L. Yang, P. Zhao, In situ self-growing 3D hierarchical BiOBr/BiOIO<sub>3</sub> Z-scheme heterojunction with rich oxygen vacancies and iodine ions as carriers transfer dual-channels for enhanced photocatalytic activity, *Chem. Eng. J.* 396 (15) (2020), 125258.
- [65] L. Li, C. Guo, J. Shen, J. Ning, Y. Zhong, Y. Hu, Construction of sugar-gourd-shaped CdS/Co<sub>1-x</sub>S hollow hetero-nanostructure as an efficient Z-scheme photocatalyst for hydrogen generation, *Chem. Eng. J.* 400 (15) (2020), 125925.
- [66] Y. Jiang, H.Y. Chen, J.Y. Li, J.F. Liao, H.H. Zhang, X.D. Wang, D.B. Kuang, Z-scheme 2D/2D heterojunction of CsPbBr<sub>3</sub>/Bi<sub>2</sub>WO<sub>6</sub> for improved photocatalytic CO<sub>2</sub> reduction, *Adv. Funct. Mater.* 30 (50) (2020) 2004293.
- [67] C. Zhang, S. Tian, F. Qin, Y. Yu, D. Huang, A. Duan, C. Zhou, Y. Yang, W. Wang, Y. Zhou, H. Luo, Catalyst-free activation of permanganate under visible light irradiation for sulfamethazine degradation: Experiments and theoretical calculation, *Water Res.* 194 (15) (2021), 116915.
- [68] F. Xu, K. Meng, B. Cheng, S. Wang, J. Xu, J. Yu, Unique S-scheme heterojunctions in self-assembled TiO<sub>2</sub>/CsPbBr<sub>3</sub> hybrids for CO<sub>2</sub> photoreduction, *Nat Commun* 11 (1) (2020) 4613.
- [69] S. Wang, X. Hai, X. Ding, K. Chang, Y. Xiang, X. Meng, Z. Yang, H. Chen, J. Ye, Light-switchable oxygen vacancies in ultrafine Bi<sub>2</sub>O<sub>3</sub>Br nanotubes for boosting solar-driven nitrogen fixation in pure water, *Adv. Mater.* 29 (31) (2017) 1701774.
- [70] D. Bao, Q. Zhang, F.L. Meng, H.X. Zhong, M.M. Shi, Y. Zhang, J.M. Yan, Q. Jiang, X.B. Zhang, Electrochemical reduction of N<sub>2</sub> under ambient conditions for artificial N<sub>2</sub> fixation and renewable energy storage using N<sub>2</sub>/NH<sub>3</sub> cycle, *Adv Mater* 29 (3) (2017) 1604799.
- [71] M. Kim, B. Lee, H. Ju, J. Kim, J. Kim, S. Lee, Oxygen-vacancy-introduced BaSnO<sub>3-δ</sub> photoanodes with tunable band structures for efficient solar-driven water splitting, *Adv. Mater.* 31 (33) (2019) 1903316.
- [72] C. Guo, K. Tian, L.i. Wang, F. Liang, F. Wang, D. Chen, J. Ning, Y. Zhong, Y. Hu, Approach of Fermi level and electron-trap level in cadmium sulfide nanorods via Molybdenum doping with enhanced carrier separation for boosted photocatalytic hydrogen production, *J. Colloid Interf. Sci.* 583 (1) (2021) 661–671.
- [73] Y. Wang, Y.u. Tian, L. Yan, Z. Su, DFT study on Sulfur-doped g-C<sub>3</sub>N<sub>4</sub> nanosheets as a photocatalyst for CO<sub>2</sub> reduction reaction, *J. Phys. Chem. C* 122 (14) (2018) 7712–7719.
- [74] L. Cheng, H. Yin, C. Cai, J. Fan, Q. Xiang, Single Ni atoms anchored on porous few-layer g-C<sub>3</sub>N<sub>4</sub> for photocatalytic CO<sub>2</sub> reduction: The role of edge confinement, *Small* 16 (28) (2020) 2002411.
- [75] J. Li, Y. Ye, L. Ye, F. Su, Z. Ma, J. Huang, H. Xie, D.E. Doronkin, A. Zimina, J.-D. Grunwaldt, Y. Zhou, Sunlight induced photo-thermal synergistic catalytic CO<sub>2</sub> conversion via localized surface plasmon resonance of MoO<sub>3-x</sub>, *J. Mater. Chem. A* 7 (6) (2019) 2821–2830.
- [76] Y. Wang, H. Arandiyán, J. Scott, K.-F. Aguey-Zinsou, R. Amal, Single atom and nanoclustered Pt catalysts for selective CO<sub>2</sub> reduction, *ACS Appl. Energy Mater.* 1 (12) (2018) 6781–6789.
- [77] Z. Ma, P. Li, L. Ye, Y. Zhou, F. Su, C. Ding, H. Xie, Y. Bai, P.K. Wong, Oxygen vacancies induced exciton dissociation of flexible BiOCl nanosheets for effective photocatalytic CO<sub>2</sub> conversion, *J. Mater. Chem. A* 5 (47) (2017) 24995–25004.
- [78] J. Sheng, Y.e. He, J. Li, C. Yuan, H. Huang, S. Wang, Y. Sun, Z. Wang, F. Dong, Identification of Halogen-associated active sites on Bismuth-based Perovskite quantum dots for efficient and selective CO<sub>2</sub>-to-CO photoreduction, *ACS Nano* 14 (10) (2020) 13103–13114.
- [79] H. Dong, S. Hong, P. Zhang, S. Yu, Y. Wang, S. Yuan, H. Li, J. Sun, G. Chen, C. Li, Metal-free Z-scheme 2D/2D VdW heterojunction for high-efficiency and durable photocatalytic H<sub>2</sub> production, *Chem. Eng. J.* 395 (1) (2020), 125150.
- [80] H. Wang, Y. Yang, Q. Li, W. Lu, J. Ning, Y. Zhong, Z. Zhang, Y. Hu, Molecule-assisted modulation of the high-valence Co<sup>3+</sup> in 3D honeycomb-like Co<sub>3</sub>S<sub>4</sub> networks for high-performance solid-state asymmetric supercapacitors, *Sci. China Mater.* 64 (4) (2021) 840–851.
- [81] H. Niu, Y. Liu, B. Mao, N. Xin, H. Jia, W. Shi, In-situ embedding MOFs-derived copper sulfide polyhedrons in carbon nanotube networks for hybrid supercapacitor with superior energy density, *Electrochim. Acta* 329 (1) (2020), 135130.